Journal of Alloys and Compounds 1074 (2026) 188778

Contents lists available at ScienceDirect

Journal of Alloys and Compounds

journal homepage: www.elsevier.com/locate/jalcom

Charge-compensated Eu^{3+} luminescence in $BaZr(BO_3)_2$: Effect of $Li^+/Na^+/K^+$ Co-doping on local symmetry, defect chemistry and radiative properties

Jabir Hakami [a], T. Karaman [b], E.A. Cin [b], O. Madkhali [a], M.B. Coban [c,d], U.H. Kaynar [e,f], B. Tas [e,f], H. Aydin [g,h], N. Can [a,*]

[a] Jazan University, College of Science, Department of Physical Sciences, Physics Division, P.O. Box 114, Jazan 45142, Kingdom of Saudi Arabia
[b] Bakircay University, Graduate School of Natural and Applied Sciences, Menemen, Izmir, Turkiye
[c] Balikesir University, Science and Technology Application and Research Center, Balikesir, Turkiye
[d] Balikesir University, Faculty of Arts and Sciences, Department of Physics, Balikesir, Turkiye
[e] Bakircay University, Faculty of Engineering and Architecture, Department of Fundamental Sciences, Menemen, Izmir, Turkiye
[f] Bakırcay University, Biomedical Technologies Design Application and Research Center, Menemen, Izmir, Turkiye
[g] Central Research Laboratories, Izmir Katip Celebi University, Izmir, Turkiye
[h] Graphene Application &Research Center, Izmir Katip Celebi University, Izmir, Turkiye

ARTICLE INFO

Keywords:
$BaZr(BO_3)_2$
Eu^{3+}-doped red phosphor
Alkali co-doping
Charge compensation
Thermal quenching / thermal stability
Near-UV/blue-excited white LEDs

ABSTRACT

$BaZr(BO_3)_2$:Eu^{3+} red phosphors were prepared via a microwave-assisted sol–gel auto-combustion approach, in which Li^+, Na^+, and K^+ ions were systematically varied and introduced as alkali co-dopants to enhance luminescence performance and provide effective charge compensation. Rietveld refinement of X-ray diffraction (XRD) data confirms the formation of a phase-pure trigonal $BaZr(BO_3)_2$ structure (space group R3c), while Fourier-transform infrared (FTIR) and Raman spectroscopy analyses reveal that the BO_3–ZrO_6 framework remains largely intact, with only slight local distortions induced by doping. Under 393 nm excitation, the phosphors display the characteristic Eu^{3+} ($^5D_0 \rightarrow {}^7F_J$) emission transitions, predominantly governed by the hypersensitive $^5D_0 \rightarrow {}^7F_2$ transition centered at approximately 612 nm, resulting in intense red emission with high color purity. The optimal Eu^{3+} concentration is determined to be 3 wt%, with concentration quenching attributed to long-range dipole–dipole interactions. Alkali-ion co-doping markedly enhances photoluminescence intensity by facilitating charge compensation and mitigating defect states. Among the introduced alkali ions, Na^+ yields the highest emission enhancement (approximately 12-fold relative to the Eu^{3+} doped sample) along with comparatively improved thermal stability, whereas K^+ effectively extends the $^5D_0$ excited-state lifetime, and Li^+ promotes increased local structural asymmetry and stronger Eu–O covalency, as evidenced by the Judd–Ofelt intensity parameter Ω_2. Temperature-dependent photoluminescence studies further suggest that the improved thermal stability in co-doped samples is associated with reduced defect-assisted non-radiative recombination pathways. These findings highlight that $Na^+/K^+/Li^+$ -compensated $BaZr(BO_3)_2$:Eu^{3+} phosphors represent promising red-emitting candidates for near-UV/blue-excited white light-emitting diodes (LEDs), where performance is critically governed by the interplay between local symmetry modulation and defect suppression mechanisms.

1. Introduction

The rapid development of solid-state lighting and display technologies has created a strong demand for efficient, thermally robust red phosphors that can be excited by near-UV or blue LED chips. Many commercial nitridosilicate and oxynitride phosphors exhibit excellent performance, but they often require complex synthesis and strict processing conditions. As a result, simpler oxide and borate hosts activated by Eu^{3+} have attracted considerable attention as cost-effective alternatives combining wide band gaps, good chemical stability and strong 4f–4 f emissions with high color purity [1–7]. Among these, Ba-based borates and perovskite-related lattices are especially promising because their flexible frameworks allow systematic tuning of local symmetry, covalency and defect structure around Eu^{3+}, thereby tailoring photoluminescence behavior and thermal stability [8–10].

$BaZr(BO_3)_2$ is a notable example of such a host, integrating ZrO_6

* Corresponding author.
E-mail address: ncan@jazanu.edu.sa (N. Can).

https://doi.org/10.1016/j.jallcom.2026.188778
Received 11 April 2026; Received in revised form 11 May 2026; Accepted 20 May 2026
Available online 21 May 2026

polyhedra and BO_3 groups in a rigid lattice that supports efficient Eu^{3+} emission under VUV and near-UV excitation, with the dominant $^5D_0 \rightarrow {}^7F_2$ transition near 615 nm and good color purity for display and lighting applications [1]. However, existing studies on $BaZr(BO_3)_2:Eu^{3+}$ and related Ba–Zr–borate systems have predominantly focused on basic excitation–emission behaviour and on co-doping strategies to boost intensity, without providing a comprehensive correlation between crystal structure, local environment and detailed Eu^{3+} photophysics [8,11,12]. In these studies, the phosphors were primarily synthesized via the conventional solid-state reaction method, which may limit precise control over particle size, homogeneity, and defect chemistry. In contrast, systematic investigations that integrate crystal structure, vibrational properties, microstructure, temperature-dependent photoluminescence, radiative dynamics, and Judd–Ofelt (J–O) parameters are still scarce. Similar integrated approaches in other Eu^{3+}-doped borates and perovskite-type hosts have proven highly effective for elucidating local structure–luminescence relationships, concentration quenching mechanisms and thermal quenching pathways, and for benchmarking new red phosphors against state-of-the-art materials for w-LEDs and plasma/field-emission devices [13–17].

In addition, incorporation of Eu^{3+} at Ba^{2+}/Zr^{4+} sites inevitably introduces charge imbalance and defect formation, particularly cation vacancies that act as non-radiative centers and deteriorate luminescence efficiency and thermal stability. A widely adopted strategy to address this issue is co-doping with monovalent alkali ions (Li^+, Na^+, K^+) as charge compensators. Previous studies on Eu^{3+}-activated phosphates and silicates have demonstrated that such A^+ co-doping can significantly enhance red emission intensity (typically by 1.2–3 ×) and improve thermal stability [18–21]. Beyond charge compensation, alkali ions modify the defect landscape by reducing vacancy concentrations and regulating oxygen-related defects, thereby suppressing non-radiative recombination and extending Eu^{3+} lifetimes [22–24]. Furthermore, partial substitution by A^+ perturbs the local coordination environment, often lowering site symmetry and increasing Eu–O covalency, which enhances the electric-dipole $^5D_0 \rightarrow {}^7F_2$ transition and Judd–Ofelt Ω_2 parameters [25,26]. Despite these advantages, such charge-compensation strategies remain largely unexplored in $BaZr(BO_3)_2:Eu^{3+}$ systems. On this basis, Na^+ and K^+ co-doping is expected not only to compensate for the $Eu^{3+} \rightarrow Ba^{2+}/Zr^{4+}$ charge mismatch, but also to tailor defect chemistry and local asymmetry around Eu^{3+}, thereby enhancing emission intensity, color purity, and thermal robustness compared with the uncompensated host.

Motivated by these gaps, the present work undertakes a systematic structural and spectroscopic investigation of Eu-doped $BaZr(BO_3)_2$ phosphors synthesized via a microwave-assisted sol–gel auto-combustion method, offering reduced particle size and improved control over compositional distribution and defect chemistry compared to conventional solid-state routes. To ensure charge compensation and stabilize Eu^{3+} incorporation into the host lattice, monovalent ions (Na^+, Li^+, and K^+) are co-introduced. The crystal structure and phase purity are established by X-ray diffraction combined with Rietveld refinement, while FTIR and Raman spectroscopy are employed to resolve the vibrational modes associated with BO_3 groups and Zr–O polyhedra and to assess lattice distortions induced by Eu incorporation. SEM/EDS analyses provide insight into morphology and elemental distribution. Steady-state photoluminescence excitation and emission spectra, together with high-temperature measurements, are used to evaluate excitation pathways, emission color characteristics and thermal quenching behavior under device-relevant conditions, in analogy with other Eu^{3+}-activated Ba-borate and Ba–Zr phosphors. Time-resolved luminescence measurements yield decay curves and lifetimes of the $^5D_0$ level, allowing separation of radiative and non-radiative contributions and assessment of concentration effects. Finally, Judd–Ofelt analysis of the Eu^{3+} emission provides intensity parameters, radiative transition probabilities, branching ratios and radiative lifetimes, linking local symmetry and covalency in $BaZr(BO_3)_2$ to its emission efficiency and enabling comparison with other Eu^{3+}-doped borate and perovskite-type red phosphors. Through this integrated approach, Eu^{3+}-doped $BaZr(BO_3)_2$ is critically evaluated as a potential red component for advanced lighting and display applications.

To the best of our knowledge, this work represents the first systematic study on $Li^+/Na^+/K^+$ charge-compensated $BaZr(BO_3)_2:Eu^{3+}$ phosphors combining time-resolved photoluminescence (TRPL) and Judd–Ofelt (J–O) analysis to elucidate the radiative and non-radiative processes. In addition, a comprehensive comparison of alkali-dependent luminescence behavior and thermal stability is presented for this host system. Furthermore, the influence of synthesis approach is addressed through a comparison between microwave-assisted sol–gel and conventional solid-state methods, providing deeper insight into structure–property relationships.

This study addresses three key questions: (i) how Eu^{3+} and $Li^+/Na^+/K^+$ co-doping modifies the crystal and vibrational structure of $BaZr(BO_3)_2$; (ii) how these changes govern room-temperature and high-temperature photoluminescence, including concentration and thermal quenching mechanisms; and (iii) whether the resulting luminescence behavior, color purity, thermal robustness, and Judd–Ofelt parameters can approach or rival those of leading Eu^{3+}-based red phosphors for near-UV/blue-pumped WLED applications.

2. Materials and methods

2.1. Synthesis of $BaZr(BO_3)_2:Eu^{3+}$ phosphors

$BaZr(BO_3)_2$ and Eu^{3+}-doped $BaZr(BO_3)_2$ phosphors were synthesized via a microwave-assisted sol–gel auto-combustion method. High-purity zirconium (IV) oxynitrate hydrate ($ZrO(NO_3)_2{\cdot}xH_2O$, Merck, ≥ 99.0%), barium nitrate ($Ba(NO_3)_2$, Sigma-Aldrich, ≥ 99.5%), and boric acid (H_3BO_3) were used as precursor materials. Europium oxide (Eu_2O_3, 99.99%, Alfa Aesar) was employed as the luminescent activator and introduced at concentrations ranging from 0.5 to 7 wt% by substitution at Ba^{2+} sites. The Eu^{3+} concentration range (0.5–7 wt%) was selected based on preliminary photoluminescence screening experiments together with previous reports on Eu^{3+}-activated borate phosphors, where concentration quenching typically occurs within a similar composition range [25]. A mixture of urea and glycine was used as the fuel for the combustion process. For the co-doping studies, lithium nitrate ($LiNO_3$, 99.9%, Merck), sodium nitrate ($NaNO_3$, 99.9%, Merck), and potassium nitrate (KNO_3, 99.9%, Merck) were incorporated into the precursor mixture at identical weight percentages to evaluate the influence of Li^+, Na^+ and K^+ ions on the structural and luminescent properties. A series of samples with varying Li^+, Na^+, and K^+ co-doping levels ($y = 0.5$–7 wt%) was systematically synthesized to evaluate the concentration-dependent effect of alkali-ion incorporation on PL enhancement and to identify the optimal co-doping level. The optimal alkali-ion concentration was determined by comparing the integrated PL emission intensities and thermal-intensity retention behavior of samples with different co-doping levels under identical excitation conditions. Among the investigated alkali ions, Na^+ co-doping at 5 wt% produced the highest emission enhancement together with comparatively improved thermal-intensity retention, and was therefore identified as the optimum charge-compensation condition for the present host lattice. In a representative synthesis procedure, stoichiometric quantities of the precursor materials were initially dissolved in 20 mL of ultrapure water using a quartz beaker. Specifically, 0.181 g of zirconium oxynitrate, 0.204 g of $Ba(NO_3)_2$, and 0.12 g of H_3BO_3 were used as the starting materials. In addition, urea and glycine were employed as combustion fuels in amounts of 0.3 g and 0.3 g, respectively. Appropriate amounts of Eu_2O_3 and alkali-ion precursors ($LiNO_3$, $NaNO_3$, or KNO_3) were subsequently added according to the designed Eu^{3+} and alkali-ion co-doping concentrations. The fuel agents (urea and glycine) were subsequently introduced into the solution, which was then covered with a watch glass and subjected to magnetic stirring at 80 °C for 1 h to ensure complete

homogenization. The resulting solution was further maintained at the same temperature under continuous stirring until a viscous gel was gradually formed due to gradual solvent evaporation.

The obtained gel was exposed to microwave irradiation using a domestic microwave oven operating at 850 W. The microwave-assisted combustion process was completed within approximately 5–7 min, during which the gel rapidly ignited and transformed into a voluminous and porous precursor powder through a self-propagating combustion reaction accompanied by the evolution of gaseous by-products [27]. To facilitate complete elimination of residual organic species and enhance crystallization, the as-combusted powders were subsequently annealed at 920 °C for 4 h under ambient air conditions [28]. Following the heat treatment, well-crystallized $BaZr(BO_3)_2$:Eu^{3+} phosphors were successfully obtained. The final products were preserved in a desiccator to avoid moisture uptake prior to subsequent characterization procedures.

Microwave-assisted sol–gel auto-combustion methods based on metal nitrates and urea-type fuels have been widely reported for the synthesis of Ba–Zr–O-based ceramic systems, including $BaZrO_3$ and related oxides [29,30]. In addition, similar nitrate–urea combustion routes have been successfully applied for the rapid preparation of Ba-containing oxide and hexaferrite nanopowders [31,32]. Furthermore, microwave-assisted synthesis has been shown to facilitate the formation of Zr–B-based ceramic precursors at relatively lower temperatures, demonstrating its effectiveness for producing borate-based phosphor materials [33].

2.2. Characterization techniques

The synthesized $BaZr(BO_3)_2$:Eu^{3+} phosphors, along with alkali co-doped counterparts, were comprehensively analyzed in terms of their structural, vibrational, morphological, and optical characteristics through a suite of complementary characterization methods.

Phase composition and crystal structure were investigated via powder X-ray diffraction (XRD) using a Malvern PANalytical Empyrean diffractometer equipped with a Cu $K\alpha_1$ radiation source ($\lambda = 1.5406$ Å). The diffraction data were collected over a 2θ range of 10°–80°, and subsequent Rietveld refinement was performed using HighScore Plus software to extract lattice parameters, evaluate phase purity, and assess structural stability. The refinements were carried out using a pseudo-Voigt peak-profile function together with a polynomial background model and a standard least-squares weighting scheme ($w_i = 1/\sigma_i^2$). The χ^2 values obtained from the refinements are close to unity and consistent with reliable refinement quality and good agreement between the observed and calculated diffraction profiles. The refinement reliability was therefore evaluated not only from χ^2 values, but also from the low R_p/R_{wp} factors, smooth residual curves, and the chemical consistency of the refined structural parameters.

Vibrational properties and local bonding configurations within the borate framework were examined by Fourier-transform infrared (FTIR) spectroscopy (Thermo Scientific Nicolet iS50) over the spectral range of 4000–400 cm^{-1}. Complementary Raman spectroscopic measurements were conducted using a Renishaw inVia system with a 532 nm excitation source, enabling detailed analysis of BO_3 units, Zr–O coordination, and local structural distortions associated with Eu^{3+} incorporation and alkali co-doping.

Microstructural characteristics and surface morphology were characterized using field-emission scanning electron microscopy (FE-SEM; ZEISS GeminiSEM 500). Elemental composition and spatial distribution were determined via energy-dispersive X-ray spectroscopy (EDS) integrated with the SEM system. Prior to imaging, the samples were coated with a thin conductive gold layer to minimize surface charging effects and enhance image clarity.

PL excitation and emission spectra were measured using an Edinburgh FS5 spectrofluorometer equipped with a 150 W xenon lamp serving as the excitation source. Time-resolved PL decay analyses were conducted to investigate the excited-state dynamics and to evaluate the average lifetimes of Eu^{3+} emission. The decay profiles were analyzed using a bi-exponential fitting model after considering the instrument response characteristics of the measurement system, and the fitting quality was evaluated using χ^2 values close to unity. Temperature-dependent PL measurements were carried out over the range of 300–500 K using a precisely controlled heating stage, enabling systematic assessment of thermal quenching characteristics and emission stability under elevated temperature conditions. To quantitatively characterize the emission color, chromaticity coordinates were derived based on the CIE 1931 colorimetric system, providing insight into color purity and correlated color temperature (CCT). To further elucidate the radiative properties and local coordination environment of Eu^{3+} ions within the $BaZr(BO_3)_2$ host lattice, a Judd–Ofelt (J–O) analysis was systematically carried out based on the emission spectral data. The obtained parameters provide quantitative insight into the asymmetry of the local crystal field and the covalency of Eu–O bonds, thereby offering a deeper understanding of the influence of alkali co-doping on the luminescence behavior.

3. Results and discussions

3.1. Crystal structure and rietveld-refined X-ray diffraction analysis

The crystal structure, phase purity, and lattice evolution of $BaZr(BO_3)_2$:Eu^{3+} and alkali co-doped phosphors were systematically investigated by powder X-ray diffraction (XRD) coupled with Rietveld refinement analysis (Fig. 1(a–c)). The samples were found to crystallize in a trigonal structure belonging to the R3c space group (hexagonal setting), which is consistent with the standard JCPDS reference card (No. 98–009–5227). The diffraction profiles of undoped, Eu^{3+}-activated, and alkali co-doped compositions (Fig. 1(a)) can be well indexed to the rhombohedral $BaZr(BO_3)_2$ phase, confirming the formation of a single-phase structure without detectable secondary phases. The distinct reflections associated with the (104), (018), (110), (024), and (112) crystallographic planes further verify the high crystallinity of the prepared samples. Notably, no appreciable peak shifts were observed upon incorporation of Eu^{3+} and alkali ions, indicating that the dopant species are effectively accommodated within the host lattice without inducing significant structural distortion.

The structural model shown in Fig. 1**(b)** confirms that $BaZr(BO_3)_2$ crystallizes in a trigonal system with space group *R3c*, derived from a distorted dolomite-type framework, consistent with previous reports [34]. The crystal structure consists of alternating BaO_6 and ZrO_6 octahedra interconnected by planar BO_3 triangular units, where rotational distortion of the BO_3 groups along the c-axis leads to a non-centrosymmetric lattice environment. In this framework, Ba^{2+} ions are coordinated by six oxygen atoms forming distorted BaO_6 polyhedra, while Zr^{4+} ions occupy relatively rigid ZrO_6 octahedral sites connected through BO_3 groups.

Considering the ionic size and charge, Eu^{3+} ions are most likely to substitute at the Ba^{2+} sites rather than Zr^{4+} sites, due to their comparable ionic radii and coordination preferences. This preferential substitution can be further supported by the ionic radius difference (D_r) calculation, where the mismatch between Eu^{3+} and Ba^{2+} is approximately 25.18%, which is below the critical limit of 30% for effective substitution, whereas the mismatch with Zr^{4+} exceeds 40%, making substitution at the Zr site energetically unfavourable [35]. Although Rietveld refinement cannot unambiguously resolve Eu^{3+} site occupancy at these low concentrations, this assignment is consistent with ionic radii, coordination preferences, and the rigidity of the ZrO_6 octahedra. Substitution at the Zr^{4+} site is energetically unfavorable because of the higher charge and smaller ionic radius of Zr^{4+}, as well as the rigidity of the ZrO_6 octahedra. The aliovalent substitution of Eu^{3+} (3^+) at Ba^{2+} (2^+) sites introduces a positive charge imbalance in the lattice. The defect chemistry related to Eu^{3+} doping can be effectively illustrated using Kröger–Vink notation. When Eu^{3+} occupies Ba^{2+} lattice sites, a charge imbalance occurs and is

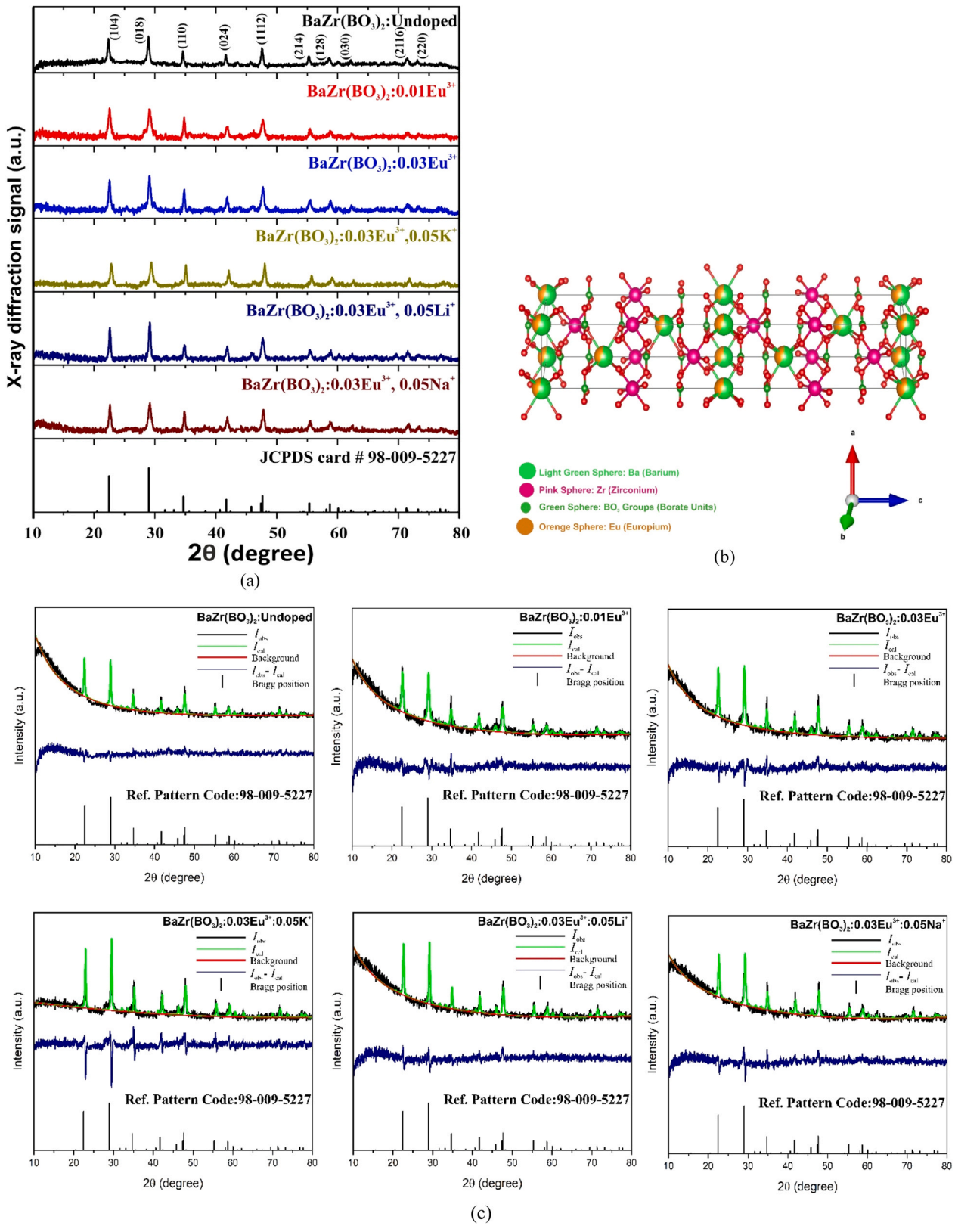

Fig. 1. (a) XRD patterns of $BaZr(BO_3)_2:Eu^{3+}$ and alkali co-doped (Li^+, Na^+, K^+) phosphors, together with the standard reference pattern (JCPDS No. 98–009-5227). All observed reflections are indexed to the rhombohedral phase, confirming phase purity and structural integrity. (b) Crystal structure model of $BaZr(BO_3)_2$, highlighting the arrangement of BaO_6 and ZrO_6 polyhedra linked by planar BO_3 units; the constituent elements and dopant sites are distinguished by different colors. (c) Rietveld refinement profiles for undoped, Eu^{3+}-doped, and alkali co-doped samples, including observed data, calculated patterns, difference curves, and Bragg positions, demonstrating excellent agreement between experimental and refined results.

compensated by the creation of cation vacancies:

$$Eu_2O_3 + 3Ba_{Ba}^{\times} \rightarrow 2Eu_{Ba}^{\bullet} + V'_{Ba} + 3BaO \quad (1)$$

where $Eu_{Ba}^{\bullet}$ denotes Eu^{3+} substituting for Ba^{2+} with an effective positive charge, while V'_{Ba} represents a doubly negatively charged barium vacancy introduced for charge compensation.

Upon co-doping with monovalent alkali ions (A^+ = Li^+, Na^+, K^+), charge compensation is achieved more effectively through:

$$Eu_2O_3 + A_2O + 4Ba_{Ba}^{\times} \rightarrow 2Eu_{Ba}^{\bullet} + 2A'_{Ba} + 4BaO \quad (2)$$

where A'_{Ba} represents monovalent alkali ions (Li^+, Na^+, K^+) substituting for Ba^{2+} sites with an effective negative charge. In this case, the $Eu_{Ba}^{\bullet} - A'_{Ba}$ defect association provides local charge compensation and suppresses the formation of vacancy-related defects. Such aliovalent substitution and defect-regulation mechanisms are widely reported for Eu-activated borate and phosphate phosphors, where such charge-compensation mechanisms reduce cation-vacancy and oxygen-related defect populations, suppress defect-assisted non-radiative relaxation pathways, and thereby enhance Eu emission intensity and thermal stability [36,37]. These defect reactions are written as physically consistent and schematic Kröger–Vink models of $Eu^{3+} \rightarrow Ba^{2+}$ substitution and alkali-ion-assisted charge compensation. While the exact defect topology cannot be directly resolved by XRD analysis alone, the proposed model is consistent with the Rietveld refinement results, Raman broadening behavior, Judd–Ofelt analysis, luminescence lifetime evolution, and thermal quenching characteristics discussed in the following sections. Although multisite Eu^{3+} occupation (simultaneous occupation of A- and B-type lattice sites) has been reported in certain perovskite-related oxide systems at high dopant concentrations, the present structural and spectroscopic results do not provide evidence for substantial Eu^{3+} incorporation at Zr^{4+} sites in $BaZr(BO_3)_2$. Significant Eu^{3+} substitution at Zr^{4+} sites would be expected to induce larger lattice distortions and more pronounced modifications of the ZrO_6–BO_3 framework. In contrast, the Rietveld refinement, Raman/FTIR spectra, and photoluminescence behavior observed in this study indicate that the trigonal R3c framework remains largely preserved with only minor local distortions. Furthermore, the Judd–Ofelt parameters, asymmetry ratios, and lifetime behavior are consistent with emission originating predominantly from a single low-symmetry Eu^{3+} environment associated mainly with Ba^{2+}-related sites. Therefore, while minor multisite occupation cannot be completely excluded at high Eu^{3+} concentrations, the combined experimental evidence supports predominantly Eu_{Ba}-type substitution with alkali-assisted charge compensation as the dominant mechanism in the investigated composition range.

This mechanism reduces the concentration of vacancy-related defects, thereby suppressing non-radiative recombination centers and enhancing luminescence efficiency.

To maintain charge neutrality, this excess positive charge is compensated by the incorporation of monovalent alkali ions (Li^+, Na^+, K^+) and/or the formation of intrinsic defects such as barium vacancies ($V''Ba$) or oxygen-related defects. In particular, the exact occupation sites of alkali ions cannot be directly resolved by XRD; however, substitution at or near Ba^{2+}-related sites is considered the most physically consistent charge-compensation model [18,38,39]. Although precise site positions cannot be directly determined from XRD analysis, the small variations in lattice parameters and the absence of secondary phases indicate that alkali ions are incorporated at low concentrations without inducing long-range structural ordering. This defect-mediated charge compensation mechanism reduces lattice strain and prevents the formation of secondary phases, which is consistent with the phase-pure XRD and Rietveld results. These defect structures will be further investigated using FTIR/Raman spectroscopy and photoluminescence (PL) lifetime analysis in the following sections.

Therefore, the combined substitution of Eu^{3+} and alkali ions establishes a charge-balanced defect structure, where local distortions are introduced without disrupting the overall crystal symmetry. Such structural asymmetry is crucial for the luminescence properties of Eu^{3+} ions, as it promotes electric dipole transitions due to the absence of inversion symmetry, consistent with previous reports. The Rietveld refinement profiles for all compositions (Fig. 1**(c)**) exhibit excellent agreement between the observed and calculated diffraction patterns, as evidenced by the close overlap of the experimental data (black circles) and the fitted curves (green line), along with minimal residuals in the difference plots.

All diffraction peaks can be attributed to the $BaZr(BO_3)_2$ phase, with no evidence of secondary phases within the detection limits of the instrument, confirming the phase purity of all samples. Furthermore, the absence of noticeable peak shifts among the samples suggests that dopant incorporation does not significantly alter the long-range crystal symmetry. Such high phase purity is crucial for the reliable interpretation of photoluminescence properties.

The refined lattice parameters, unit-cell volumes, and refinement reliability factors are summarized in Table 1, together with the Rietveld refinement profiles shown in (Fig. 1(c)), further support the structural stability of the system. Although the ionic radius of Eu^{3+} (~1.07 Å) is smaller than that of Ba^{2+} (~1.35 Å), the slight increase in the refined unit-cell volume with increasing Eu^{3+} concentration does not necessarily contradict the proposed substitution mechanism. In aliovalent substitution systems, the lattice response is governed not only by ionic size but also by local structural relaxation, charge-compensation mechanisms, and defect formation. When Eu^{3+} substitutes for Ba^{2+}, the resulting charge imbalance may induce cation vacancies and local distortions of the surrounding coordination environment, which may slightly expand the average lattice framework despite the smaller Eu^{3+} ionic radius. Similar anomalous lattice-expansion behavior has been reported in several Eu^{3+}-doped oxide and borate phosphor systems, where defect-assisted relaxation competes with the simple ionic-size effect. It should also be noted that the variation in the refined cell volume is relatively small and does not follow a simple ionic-radius trend, indicating that local structural relaxation and defect-compensation effects play an important role in determining the average lattice response [38].

In contrast, alkali co-doping induces slight but noticeable changes in the unit cell volume, where Li^+ incorporation leads to lattice expansion (≈ 787.10 Å^3), Na^+ results in moderate expansion (≈ 784.66 Å^3), and K^+ causes a slight contraction (≈ 781.04 Å^3). This behavior suggests that Li^+-induced lattice expansion may be associated with interstitial incorporation and/or vacancy formation, whereas the slight contraction observed for K^+ is consistent with partial substitution at Ba^{2+} sites accompanied by reduced vacancy concentration. These variations can be explained based on ionic size and charge compensation effects; Li^+ (0.76 Å), Na^+ (1.02 Å), and K^+ (1.38 Å) introduce different degrees of local strain and defect formation when incorporated into the lattice or interstitial positions. Despite these small variations, the absence of significant changes in lattice constants and peak positions indicates that the structural distortions remain minimal, confirming the robustness of the $BaZr(BO_3)_2$ framework against both Eu^{3+} substitution and alkali co-doping. This structural stability highlights the suitability of $BaZr(BO_3)_2$ as an efficient host lattice for Eu^{3+} activator ions.

The refinement reliability indicators fall within acceptable limits (R_p=0.0488–0.0679, R_{wp}=0.0609–0.1007, χ^2=1.0032–1.4252), confirming the high quality of the refinement and the validity of the structural model. In particular, the relatively small difference between the R_{wp} and R_{exp} values together with χ^2 values close to unity indicate an excellent agreement between the observed and calculated diffraction patterns, demonstrating that the chosen structural model accurately represents the experimental data. This level of agreement ensures that further structural interpretations, such as site occupancy and lattice parameter variations, are reliable. Moreover, no significant anisotropic peak broadening was observed in the refinement profiles, suggesting

Table 1
Refined lattice parameters (*a*, *b*, *c*), unit cell volume, and Rietveld refinement reliability factors (χ^2, R_p, R_{wp}, and R_{exp}) of $BaZr(BO_3)_2$:Eu^{3+} and alkali co-doped samples (Li^+, Na^+, K^+), obtained from the Rietveld analysis of X-ray diffraction data.

	$BaZr(BO_3)_2$					
Unit Cell	**Undoped**	**0.01Eu^{3+}**	**0.03Eu^{3+}**	**0.03Eu^{3+},0.05 K^+**	**0.03Eu^{3+},0.05Li^+**	**0.03Eu^{3+},0.05Na^+**
a [Å]	5.1676	5.17065	5.17258	5.15947	5.1751	5.17385
b [Å]	5.1676	5.17065	5.17258	5.15947	5.1751	5.17385
c [Å]	33.83733	33.85749	33.86027	33.87927	33.93627	33.84746
α,β,γ [°]	90,90,120	90,90,120	90,90,120	90,90,120	90,90,120	90,90,120
Vol. [$Å^3$]	782.535	783.9358	784.5772	781.0416	787.103	784.6643
χ^2	1.1013	1.0032	1.0975	1.4252	1.0296	1.0554
R_p	0.0548	0.0488	0.0490	0.0679	0.0532	0.0531
R_{wp}	0.0676	0.0609	0.0624	0.1007	0.0664	0.0668
R_{exp}	0.0614	0.0607	0.0626	0.0706	0.0644	0.0633

that microstrain effects are minimal. However, slight peak broadening in the co-doped samples may indicate the presence of local lattice distortions and defect-induced strain, which can be associated with charge compensation mechanisms and may influence the photoluminescence behavior of the phosphor system.

This site assignment is further supported by the composition-dependent changes in lattice parameters (Table 1), Judd–Ofelt parameters (Tables 7, 8), and luminescence lifetimes (Fig. 9). The preferential occupation sites of Eu^{3+} and alkali ions in the $BaZr(BO_3)_2$ lattice can be rationalized according to ionic radius, charge balance, and local coordination environment. Considering ionic radius, valence state, and coordination environment, Eu^{3+} ions are more likely to substitute for Ba^{2+} lattice sites rather than Zr^{4+} sites in the $BaZr(BO_3)_2$ host lattice. The ionic radius mismatch (Δr) between Eu^{3+} (1.066 Å, CN = 8) and Ba^{2+} (1.42 Å, CN = 8) is approximately 25%, which is below the generally accepted ~30% substitution criterion based on the Hume–Rothery rule, whereas the mismatch between Eu^{3+} and Zr^{4+} exceeds 40%, making Eu^{3+}→Zr^{4+} substitution energetically unfavorable [40].

The ionic radius mismatch (Δr) between Eu^{3+} (1.066 Å, CN = 8) and Ba^{2+} (1.42 Å, CN = 8) was calculated using the following relation [41]:

$$D_r = \frac{|R_m(CN) - R_d(CN)|}{R_m(CN)} \times 100\% \quad (3)$$

where R_m(CN) and R_d(CN) represent the ionic radii of the matrix cation and dopant ion, respectively, for the same coordination number (CN). The ionic radii were taken from Shannon's effective ionic radii database. Using CN = 8 for both Ba^{2+} and Eu^{3+} ions, the calculated mismatch is approximately 25%, which is below the generally accepted ~30% substitution criterion based on the Hume–Rothery rule, whereas the mismatch between Eu^{3+} and Zr^{4+} exceeds 40%, making Eu^{3+}→Zr^{4+} substitution energetically unfavorable.

In addition, Eu^{3+} substitution at the Ba^{2+} site requires only local charge compensation, while substitution at the Zr^{4+} site would induce simultaneous charge imbalance and severe lattice distortion due to both valence and size mismatch. Similarly, the alkali ions (Li^+, Na^+, and K^+) are expected to preferentially occupy nearby Ba^{2+} sites and/or interstitial positions to compensate for the excess positive charge generated by Eu^{3+}→Ba^{2+} substitution. This assignment is supported by the systematic variation observed in lattice distortion, Judd–Ofelt intensity parameters, luminescence lifetime, and thermal stability after alkali-ion incorporation. The significant enhancement in emission intensity together with the suppression of non-radiative relaxation pathways further indicates that alkali-ion co-doping effectively regulates defect formation and local symmetry around Eu^{3+} ions [22,42].

Overall, XRD and Rietveld refinement results reveal that the trigonal (R3c) framework of $BaZr(BO_3)_2$ remains intact upon Eu^{3+} doping and alkali co-doping, with minor local distortions that contribute to the modulation of optical properties. Furthermore, the sol–gel auto-combustion synthesis promotes the formation of uniform single-phase materials, effectively suppressing impurity phases commonly encountered in conventional solid-state routes.

3.2. FTIR and Raman spectroscopic analysis

The vibrational properties and local bonding environment of $BaZr(BO_3)_2$:Eu^{3+} and alkali co-doped phosphors were analyzed using FTIR and Raman spectroscopy (Fig. 2**(a, b)**). The FTIR spectra exhibit characteristic absorption features of borate groups, including a broad band at 1209–1421 cm^{-1} corresponding to asymmetric stretching modes of trigonal BO_3 units. The band near ~998 cm^{-1} is associated with B–O stretching vibrations, while those at ~725 and ~610 cm^{-1} originate from bending modes of B–O–B linkages. Additionally, the low-frequency band around ~401 cm^{-1} is attributed to lattice vibrations involving Ba–O and Zr–O bonds [4,43]. These features confirm the formation of a borate framework consistent with the crystal structure identified by XRD analysis. These modes are consistent with the presence of isolated trigonal BO_3 groups and corner-sharing BaO_6/ZrO_6 polyhedra in $BaZr(BO_3)_2$ [44].

Importantly, no additional absorption related to impurity phases is observed, further supporting the phase purity of the samples, in agreement with XRD and Rietveld results. Upon Eu^{3+} doping and alkali co-doping, no significant changes in peak positions are detected, indicating that the fundamental BO_3 framework remains structurally intact. However, slight variations in band intensity and minor broadening are observed, suggesting the presence of local lattice distortions induced by dopant incorporation and charge compensation mechanisms [45–47].

Raman spectroscopy provides complementary insight into the short-range order and local structural distortions around BO_3 units and metal–oxygen polyhedral, as shown in Fig. 2**b**. The prominent Raman modes observed at ~371 cm^{-1}, ~481 cm^{-1}, ~619 cm^{-1}, ~738 cm^{-1}, and ~1063–1229 cm^{-1} are characteristic of BO_3 vibrational units and lattice modes associated with Ba and Zr coordination environments [27,48]. The strong peak near ~1063–1229 cm^{-1} corresponds to symmetric stretching vibrations of BO_3 groups, while lower-frequency modes are related to bending and lattice vibrations. These vibrational features are characteristic of trigonal BO_3 units and are consistent with the borate framework identified by XRD analysis.

Similar to the FTIR results, no additional Raman peaks corresponding to secondary phases are detected, confirming the structural stability of the host lattice upon doping. The slight broadening and intensity variation of Raman peaks in co-doped samples indicate the presence of local structural disorder and defect-induced strain, which are consistent with the Rietveld refinement and lattice parameter analysis.

Overall, the combined FTIR and Raman analyses confirm that the borate framework of $BaZr(BO_3)_2$ is preserved after Eu^{3+} substitution and alkali co-doping, with only minor local distortions that do not affect the long-range crystal symmetry but may play a significant role in tuning the optical properties of the phosphor system. The observed Raman features further support the presence of a non-centrosymmetric local environment around Eu^{3+} ions, which is crucial for enhancing electric dipole transitions and thus correlates with the observed photoluminescence

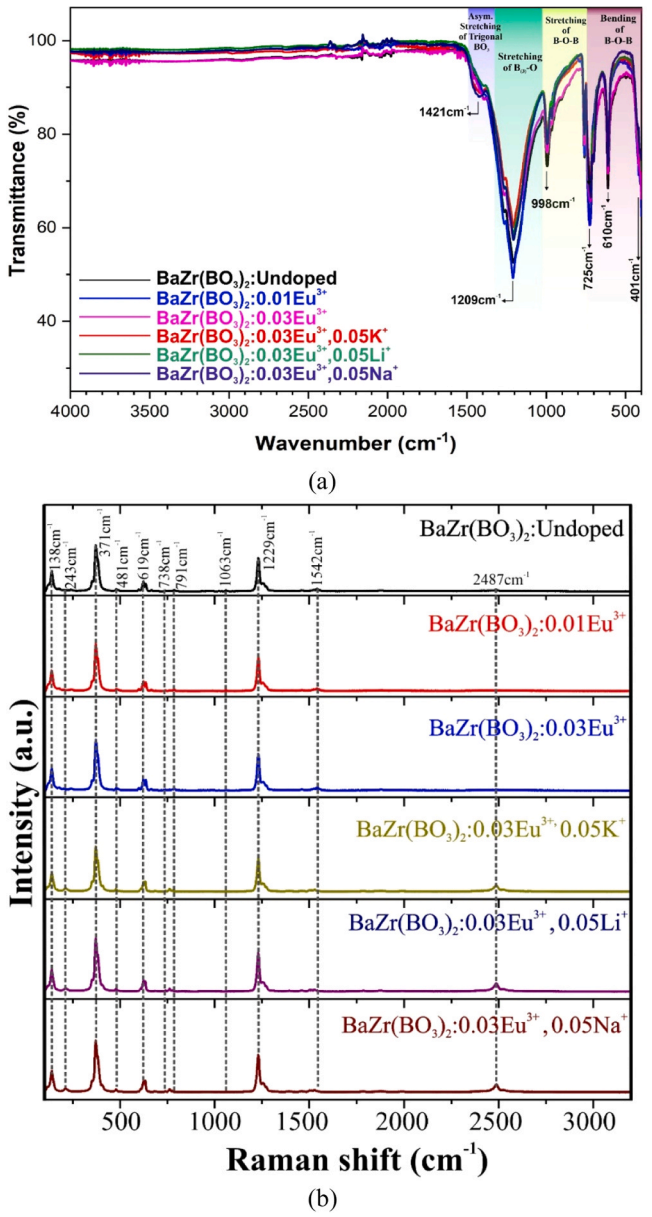

Fig. 2. (a) FTIR spectra and (b) Raman spectra of $BaZr(BO_3)_2$:Undoped, $BaZr(BO_3)_2$:0.01Eu^{3+}, $BaZr(BO_3)_2$:0.03Eu^{3+}, and $BaZr(BO_3)_2$:0.03Eu^{3+},0.05 A^+ ($A = K^+$, Li^+, Na^+) phosphors. The FTIR spectra display characteristic vibrations of BO_3 units, while the Raman spectra confirm the borate framework.

behavior [49,50].

To quantitatively evaluate the peak broadening induced by Eu^{3+} and alkali-ion co-doping, the full width at half maximum (FWHM) values of the major Raman modes were extracted and are summarized in Table 2. Compared with the undoped $BaZr(BO_3)_2$ sample, the co-doped phosphors generally exhibit slightly increased FWHM values, particularly for the modes associated with BO_3 vibrations and lattice-related phonon modes. This broadening indicates increased local structural disorder, lattice distortion, and phonon perturbation induced by aliovalent Eu^{3+} substitution and alkali-ion incorporation. The relatively larger FWHM values observed for Li^+- and Na^+-co-doped samples are consistent with enhanced local asymmetry and defect-regulated lattice distortion discussed in the photoluminescence and Judd–Ofelt analyses.

3.3. Morphological and elemental analysis (SEM–EDS)

The surface morphology of the synthesized $BaZr(BO_3)_2$:Eu^{3+} phosphors was examined by scanning electron microscopy (SEM), as shown in Fig. 3**(a,b)**. At low magnification, all compositions investigated, including Eu^{3+} and alkali co-doped samples, exhibit irregular and agglomerated particle morphology, which is typical for phosphors synthesized via sol–gel auto-combustion routes. This agglomeration is attributed to the rapid evolution of gaseous by-products during combustion, leading to the formation of loosely packed particle clusters.

At higher magnification, the particles appear as fused grains with rough surfaces, indicating partial sintering and grain growth during the combustion process. The absence of well-defined faceted structures suggests diffusion-limited crystal growth. Such features indicate a polycrystalline nature, which is consistent with the phase-pure and well-crystallized $BaZr(BO_3)_2$ lattice revealed by XRD and Rietveld refinement analysis.

The elemental composition was analyzed by energy-dispersive X-ray spectroscopy (EDS), as shown in the insets of Fig. 3**(a,b)**. The EDS spectra reveal Ba, Zr, and O in the undoped sample and Ba, Zr, O, and Eu in the Eu^{3+}-doped sample, without impurity-related peaks, indicating chemical purity within the detection limits of the technique and supporting the phase-pure XRD/Rietveld results. The relatively weak Eu signal is attributed to the low doping concentration.

Overall, the samples exhibit morphologically similar particles and chemically homogeneous composition within the spatial resolution and detection limits of SEM–EDS. Such chemically pure and structurally consistent phosphor particles provide a suitable basis for the stable and efficient Eu^{3+} photoluminescence discussed in Sections 3.4–3.7.

3.4. Photoluminescence excitation and emission properties

The PLE and PL spectra of $BaZr(BO_3)_2$:Eu^{3+} phosphor are presented in Fig. 4**a**. The excitation spectrum monitored at 612 nm reveals a broad band centered at ~257 nm, corresponding to the O^{2-}→Eu^{3+} charge transfer transition and indicating efficient energy transfer from the host matrix to Eu^{3+} ions [2,51,52]. Superimposed on this band are several

Table 2
Raman peak full width at half maximum (FWHM) values of undoped, Eu^{3+}-doped, and alkali co-doped $BaZr(BO_3)_2$ phosphors.

			$BaZr(BO_3)_2$	(FWHM)		
Wavenumber (cm^{-1})	Undoped	0.01Eu^{3+}	0.03Eu^{3+}	0.03Eu^{3+},0.05 K^+	0.03Eu^{3+},0.05Li^+	0.03Eu^{3+},0.05Na^+
138	15.81316	16.20615	16.02765	18.12787	17.76061	18.62064
243	43.43591	50.17897	46.92715	49.58536	44.3764	44.71366
371	21.52987	21.75675	21.64189	22.09265	22.10924	22.15841
481	18.99498	20.89338	19.13712	19.13712	19.49049	19.73643
619	12.07025	12.77438	12.62255	12.80457	12.94559	12.53594
738	9.39795	10.21246	10.36236	10.36463	10.90547	10.08689
791	17.56016	20.55292	19.84152	19.84152	20.27591	20.35308
1063	7.152799	7.77764	12.40352	12.44291	12.50142	12.37516
1229	15.24583	15.72578	15.08786	15.29914	15.67866	15.47563
1542	22.15274	25.61111	23.26522	23.29133	25.35784	25.16024
2487	44.14189	45.04883	42.02933	47.25293	48.42393	48.37963

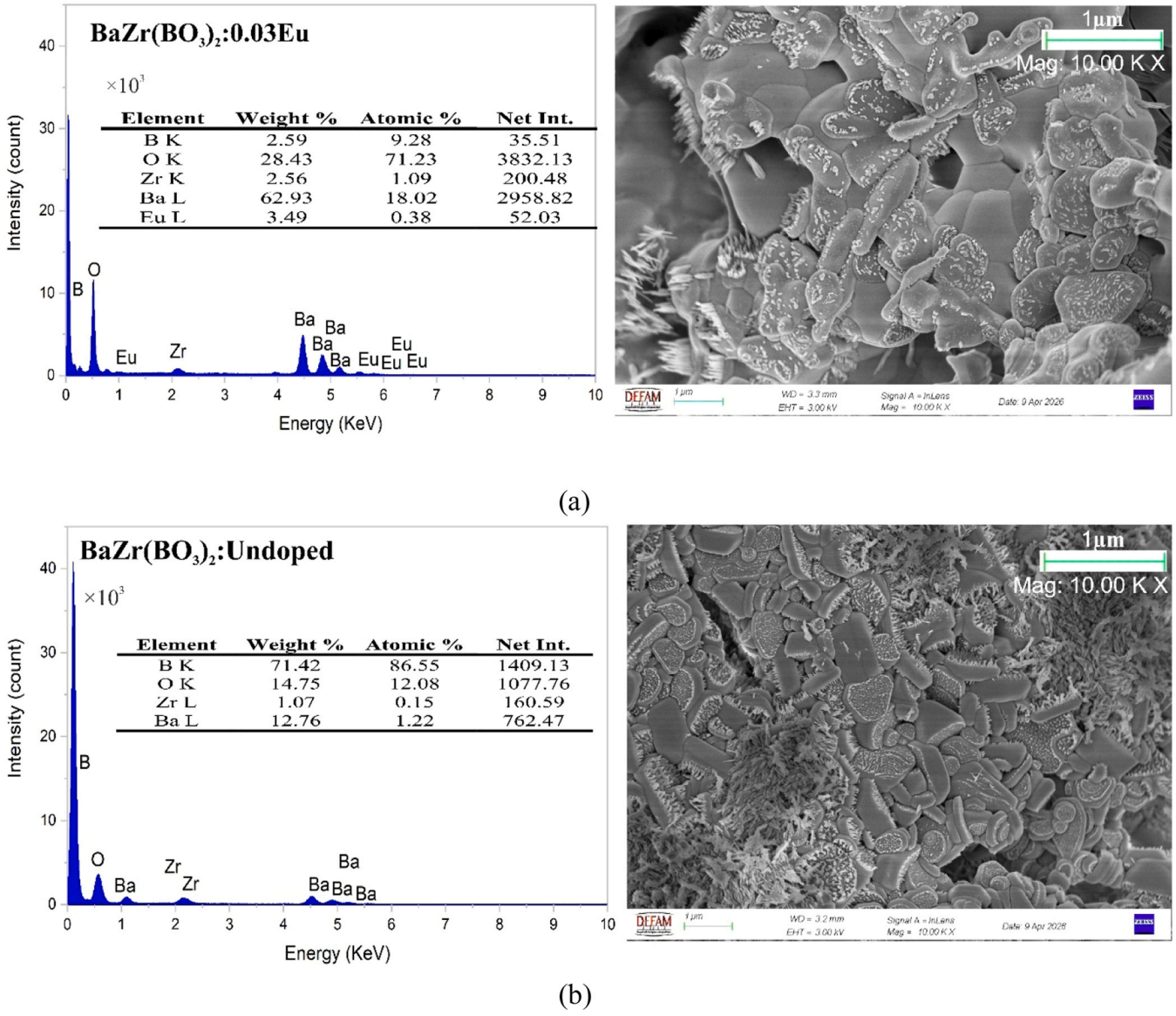

Fig. 3. SEM images of (a) $BaZr(BO_3)_2$ and (b) $BaZr(BO_3)_2$:3 wt% Eu^{3+} phosphors, showing agglomerated particle morphology. The insets in (a) and (b) show the corresponding EDS spectrum, confirming the elemental composition.

sharp peaks arising from intra-4f electronic transitions of Eu^{3+}, located at 319 nm ($^7F_0 \rightarrow {}^5H_6$), 362 nm ($^7F_0 \rightarrow {}^5D_4$), 376 nm ($^7F_0 \rightarrow {}^5L_7$), 393 nm ($^7F_0 \rightarrow {}^5L_6$), 415 nm ($^7F_0 \rightarrow {}^5D_3$), and 464 nm ($^7F_0 \rightarrow {}^5D_2$) [53,54]. Among these, the 393 nm transition dominates the excitation profile, confirming the effectiveness of near-UV excitation for this phosphor system.

Upon excitation at 393 nm, the emission spectrum displays characteristic Eu^{3+} emissions arising from the $^5D_0$ excited state to the ^7F_J (J = 0–4) levels. The observed emission peaks at 572 nm ($^5D_0 \rightarrow {}^7F_0$), 594 nm ($^5D_0 \rightarrow {}^7F_1$), 612 nm ($^5D_0 \rightarrow {}^7F_2$), 654 nm ($^5D_0 \rightarrow {}^7F_3$), and 702 nm ($^5D_0 \rightarrow {}^7F_4$) confirm the successful incorporation of Eu^{3+} ions into the host lattice [17,51]. The $^5D_0 \rightarrow {}^7F_2$ emission band in the 610–620 nm region exhibits Stark splitting, with the most intense component located at ~612 nm, reflecting crystal field-induced splitting of the hypersensitive transition [8]. The $^5D_0 \rightarrow {}^7F_2$ transition exhibits a limited number of Stark components, further supporting the presence of a single dominant Eu^{3+} site with low symmetry in the host lattice. The dominance of the electric-dipole $^5D_0 \rightarrow {}^7F_2$ transition over the magnetic-dipole $^5D_0 \rightarrow {}^7F_1$ line ($I_{612}/I_{594} = 2.18$) indicates that Eu^{3+} ions preferentially occupy Ba^{2+} sites lacking inversion symmetry in the $BaZr(BO_3)_2$ lattice, consistent with previous reports [2,55,56].

The strong $^5D_0 \rightarrow {}^7F_2$ emission results in intense red luminescence with high color purity, which is desirable for photonic applications. The relatively weak $^5D_0 \rightarrow {}^7F_0$ transition further suggests a limited number of distinct crystallographic sites for Eu^{3+} ions, which is consistent with the limited number of Stark components observed for the $^5D_0 \rightarrow {}^7F_2$ transition. The emission profiles recorded under different excitation wavelengths (247–464 nm) exhibit identical spectral features with consistent relative intensities of the $^5D_0 \rightarrow {}^7F_J$ transitions, indicating excitation-independent emission behavior. This suggests that the emission originates from a single dominant Eu^{3+} site and that different excitation pathways efficiently relax to the same emitting $^5D_0$ level.

Fig. 4**b** shows the emission spectra of $BaZr(BO_3)_2$:3 wt%Eu^{3+} under excitation between 247 and 464 nm. All spectra display nearly identical $^5D_0 \rightarrow {}^7F_J$ (J = 0–4) profiles with only minor variations in relative peak intensities, indicating that the emission originates from the same $^5D_0$ excited state of Eu^{3+} ions regardless of the excitation pathway. This behavior suggests that different excitation channels, including the $O^{2-} \rightarrow Eu^{3+}$ charge-transfer band and intra-configurational 4f–4 f transitions, efficiently relax to the same emitting level.

It should be noted that the relative intensities of the 393 and 464 nm

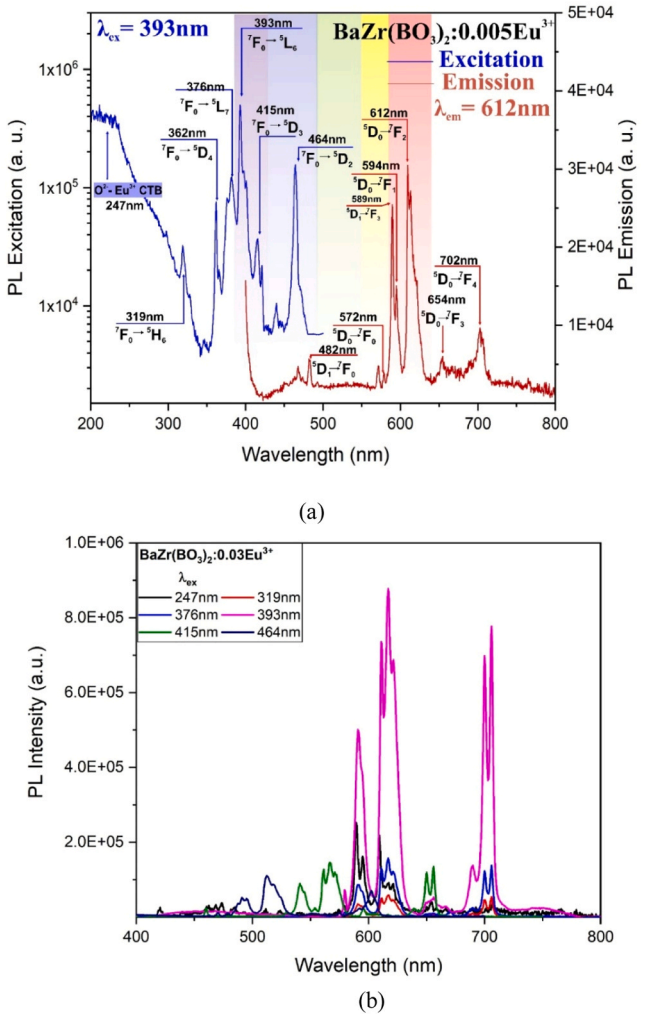

Fig. 4. (a) PL excitation and emission spectra of $BaZr(BO_3)_2$:0.5 wt% Eu^{3+} phosphor. (b) Emission spectra of $BaZr(BO_3)_2$:3 wt% Eu^{3+} phosphor measured under varying excitation wavelengths (247–464 nm), demonstrating excitation-independent spectral profiles alongside excitation-dependent emission intensities.

bands in the excitation spectrum differ from the corresponding emission intensities observed in the PL spectra because the two measurements probe different physical processes. The PLE spectrum was recorded by monitoring the 612 nm emission and therefore reflects the relative efficiency of different excitation transitions populating the Eu^{3+} $^5D_0$ emitting level, whereas the PL spectra represent the radiative relaxation behavior from the populated $^5D_0$ state under different excitation wavelengths. Consequently, the relative peak heights in the PLE spectrum are not expected to directly match the emission intensities in the PL spectra. The apparent difference between the emission spectra obtained under 393 and 415 nm excitation mainly originates from the different absorption strengths of the Eu^{3+} $^7F_0 \rightarrow {}^5L_6$ and $^7F_0 \rightarrow {}^5D_3$ transitions, together with the spectral normalization applied in Fig. 4. Nevertheless, the characteristic Eu^{3+} $^5D_0 \rightarrow {}^7F_j$ emission pattern remains essentially unchanged, confirming that both excitation pathways ultimately relax to the same $^5D_0$ emitting state.

In contrast, the emission intensity varies significantly with excitation wavelength, reaching a maximum under 393 nm excitation ($^7F_0 \rightarrow {}^5L_6$). Excitation at 464 nm ($^7F_0 \rightarrow {}^5D_2$) also yields appreciable emission intensity, demonstrating that the phosphor can be efficiently excited by both near-UV and blue light sources. This feature is particularly beneficial for solid-state lighting applications, as these excitation wavelengths are compatible with commonly used near-UV and blue LED chips [57,58].

Overall, the spectral features demonstrate that $BaZr(BO_3)_2$ provides a suitable host environment for Eu^{3+}, enabling efficient red emission under near-UV excitation. Furthermore, the relatively high asymmetry ratio (2.18) indicates enhanced electric-dipole transition probability and increased local asymmetry around Eu^{3+} ions. This interpretation will be further supported by the Judd–Ofelt analysis presented in a later section, where the relatively high Ω_2 parameter and enhanced electric-dipole transition probability provide evidence for a low-symmetry environment around Eu^{3+} ions. In addition, lifetime analysis offers further insight into the interplay between radiative and non-radiative processes governing the emission behavior.

3.5. Concentration-dependent photoluminescence and quenching behavior

The emission spectra of $BaZr(BO_3)_2$:$x$$Eu^{3+}$ under 393 nm excitation, are presented in Fig. 5**a**. With increasing Eu^{3+} content from 0.5 to 3 wt %, the emission intensity increases progressively and reaches a maximum at 3 wt%, followed by a decline at higher concentrations (5–7 wt%), indicating the onset of concentration quenching. This behaviour is characteristic of Eu^{3+}-activated borate and oxide phosphors, where non-radiative energy transfer among neighbouring Eu^{3+}

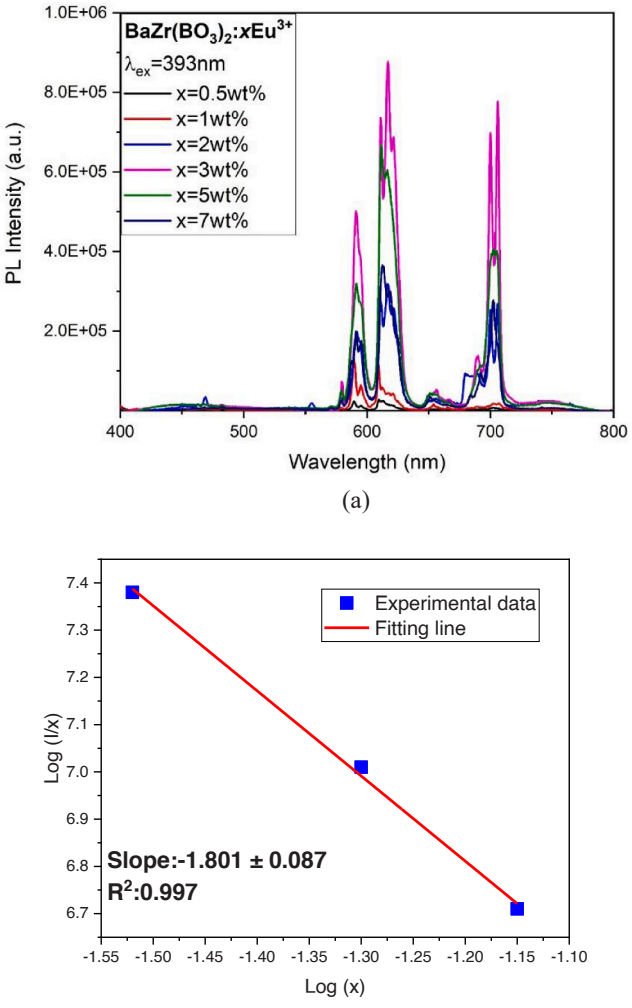

Fig. 5. (a) PL emission spectra of $BaZr(BO_3)_2$:$x$$Eu^{3+}$ phosphors (x = 0.5–7 wt%) under 393 nm excitation (b) Dexter-type analysis of concentration quenching in $BaZr(BO_3)_2$:$x$$Eu^{3+}$ phosphors: plot of log(I/x) versus log(x) with linear fitting.

ions becomes dominant beyond a critical concentration [59–61].

Importantly, the spectral profiles remain nearly unchanged with increasing Eu^{3+} content, and all samples exhibit characteristic $^5D_0 \rightarrow {}^7F_J$ ($J = 0$–4) transitions. The dominance of the $^5D_0 \rightarrow {}^7F_2$ transition over the $^5D_0 \rightarrow {}^7F_1$ transition is preserved across all concentrations, indicating that Eu^{3+} ions occupy similar crystallographic sites and that the local symmetry around Eu^{3+} ions is not significantly altered by concentration. This suggests that the quenching process primarily affects emission intensity rather than the emission mechanism.

To further evaluate the local environment of Eu^{3+} ions, the asymmetry ratio $I(^5D_0 \rightarrow {}^7F_2) / I(^5D_0 \rightarrow {}^7F_1)$ was analyzed as a function of Eu^{3+} concentration. The ratio varies non-monotonically from 1.35 to 2.12 across the composition range, while remaining consistently greater than unity, confirming that Eu^{3+} ions predominantly occupy non-centrosymmetric sites. The decrease in the asymmetry ratio at intermediate concentrations (2–3 wt%) followed by an increase at higher concentrations (5–7 wt%) suggests a concentration-dependent modification of the local crystal field around Eu^{3+} ions. Similar concentration-dependent, non-monotonic variations of asymmetry ratio or Ω_2 have been reported in perovskite and oxide hosts, where they are attributed to a competition between lattice relaxation, defect formation, and evolving Eu–defect configurations rather than a simple monotonic trend in symmetry [57,62,63].

The decline in emission intensity at higher Eu^{3+} concentrations is attributed to concentration quenching mediated by non-radiative energy transfer. The estimated critical distance ($R_p \approx 29.24$ Å), based on Blasse's approach, is substantially larger than the 3–5 Å range characteristic of exchange interactions, thereby excluding exchange mechanisms and pointing to long-range multipolar interactions as the dominant quenching pathway. In such systems, excitation energy migrates through Eu^{3+} ion networks and is eventually dissipated via non-radiative relaxation, reducing the overall emission efficiency. Nevertheless, it should be noted that the asymmetry ratio is a semi-quantitative indicator of local symmetry and does not provide definitive evidence for site redistribution or multiple Eu^{3+} environments. Multisite occupation or defect-related Eu^{3+} environments may lead to non-monotonic variations in the asymmetry ratio, as reported in other Eu^{3+}-activated host lattices [57,64]. Such interpretations are consistent with the Judd–Ofelt analysis presented in Section 3.9, where variations in the Ω_2 parameter confirm changes in the local asymmetry around Eu^{3+} ions. In addition, the lifetime analysis supports the presence of competing radiative and non-radiative processes contributing to the observed concentration-dependent behavior.

These results indicate that an optimal Eu^{3+} concentration of approximately 3 wt% provides the best balance between emission intensity and quenching effects, making it the most suitable composition for further photophysical and device-related investigations.

To further elucidate the quenching mechanism, the critical distance (R_c) between Eu^{3+} ions was estimated using Blasse's formula [65]:

$$R_c = 2\left[\frac{3V}{4\pi x_c N}\right]^{1/3} \quad (4)$$

where V is the unit cell volume (784.58 Å^3), N is the number of available cation sites per unit cell (2), and x_c is the critical concentration corresponding to the onset of concentration quenching, i.e., the Eu^{3+} content at which the PL intensity reaches its maximum and begins to decrease (in this case, ~3 wt%). The calculated critical distance R_c (~29.23 Å) is significantly larger than the 3–5 Å range typically associated with exchange interaction, indicating that exchange-mediated energy transfer is unlikely to dominate in $BaZr(BO_3)_2{:}xEu^{3+}$. Similar conclusions have been reported in Eu^{3+}-activated oxides and borates, where large R_c values (>10 Å) indicate that electric multipolar interactions are the primary mechanism responsible for concentration quenching [66,67]. Under these conditions, concentration quenching is mainly controlled by long-range multipolar interactions between Eu^{3+} ions, facilitating energy migration across adjacent sites and subsequent dissipation through non-radiative processes, thereby reducing luminescence efficiency [68,69].

To gain deeper insight into the multipolar interaction mechanism responsible for concentration quenching, a Dexter-type analysis was conducted by plotting $\log(I/x)$ as a function of $\log(x)$, as illustrated in Fig. 5**b**. Linear fitting of the experimental data yields a slope of -1.801 ± 0.088 with an excellent correlation coefficient ($R^2 = 0.998$). According to Dexter theory, the obtained slope corresponds to a θ value of 5.40 ± 0.26, which is close to the theoretical value of $\theta = 6$ expected for dipole–dipole interactions. These results therefore indicate that the concentration quenching process in $BaZr(BO_3)_2{:}Eu^{3+}$ is predominantly governed by long-range dipole–dipole energy transfer between neighboring Eu^{3+} ions. Similar dipole–dipole-controlled concentration quenching behavior has been widely reported in Eu^{3+}-activated oxide and borate phosphor systems.

3.6. Influence of alkali Co-doping (Li^+, Na^+, K^+) on the photoluminescence properties of $BaZr(BO_3)_2{:}Eu^{3+}$ phosphors

The influence of alkali ion co-doping (Li^+, Na^+, and K^+) on the photoluminescence (PL) properties of $BaZr(BO_3)_2$:3 wt% Eu^{3+} phosphors under 393 nm excitation is illustrated in Fig. 6(a–c). For all co-doped compositions, the emission spectra exhibit the characteristic Eu^{3+} ($^5D_0 \rightarrow {}^7F_J$, $J = 0$–4) transitions with nearly identical spectral profiles, indicating that the introduction of alkali ions does not significantly modify the intrinsic emission mechanism or the energy levels of Eu^{3+} ions. This observation is consistent with previously reported Eu^{3+}-activated borate and oxide phosphor systems, where alkali ion co-doping ($A^+ = Li^+$, Na^+, K^+) enhances emission intensity without altering the fundamental $^5D_0 \rightarrow {}^7F_J$ spectral features. These results confirm that the luminescence process remains unchanged, while the enhancement in emission intensity is primarily attributed to improved local structural environment and defect compensation effects induced by alkali incorporation [26,70–72]. However, significant differences in emission intensity are observed depending on the type and concentration of alkali ions. In all cases, the PL intensity initially increases with increasing alkali content, reaches a maximum at an optimal concentration, and then decreases at higher doping levels, suggesting that charge compensation plays a crucial role in enhancing luminescence efficiency.

Among the three alkali ions, Na^+ co-doping provides the most pronounced enhancement in emission intensity, achieving approximately 12-fold higher PL intensity at the optimal concentration compared to the 3 wt% Eu^{3+} doped sample (Fig. 6**b**), whereas K^+ shows a moderate improvement (Fig. 6**a**) and Li^+ exhibits the weakest effect (Fig. 6**c**). This trend can be rationalized by considering the relative ionic size and lattice compatibility of the co-dopant ions. In particular, Na^+ provides optimal enhancement due to its favorable ionic radius, which closely matches that of Ba^{2+}, enabling efficient substitution and effective charge compensation of Eu^{3+}-induced defects [18,21,71]. In contrast, the smaller Li^+ ion may introduce local lattice distortion or occupy interstitial sites, while the larger K^+ ion may induce excessive lattice strain at higher concentrations, both of which can limit emission enhancement [13,42,73].

Such behavior is consistent with previous studies on Eu^{3+}-activated phosphors, where the effectiveness of alkali co-doping strongly depends on the ionic radius match between the co-dopant and host cation sites. In many borate and oxide systems, Na^+ often yields the highest luminescence enhancement due to its balanced size and efficient defect compensation, whereas Li^+ and K^+ may lead to lattice distortion or secondary phase formation at higher concentrations [18,21,72].

For clarity, the typical roles of different alkali co-dopants in Eu^{3+}-activated phosphors are summarized in Table 3. The present results are in good agreement with these general trends, particularly highlighting the superior role of Na^+ in the $BaZr(BO_3)_2$ host.

The superior performance of Na^+ can be attributed to its more

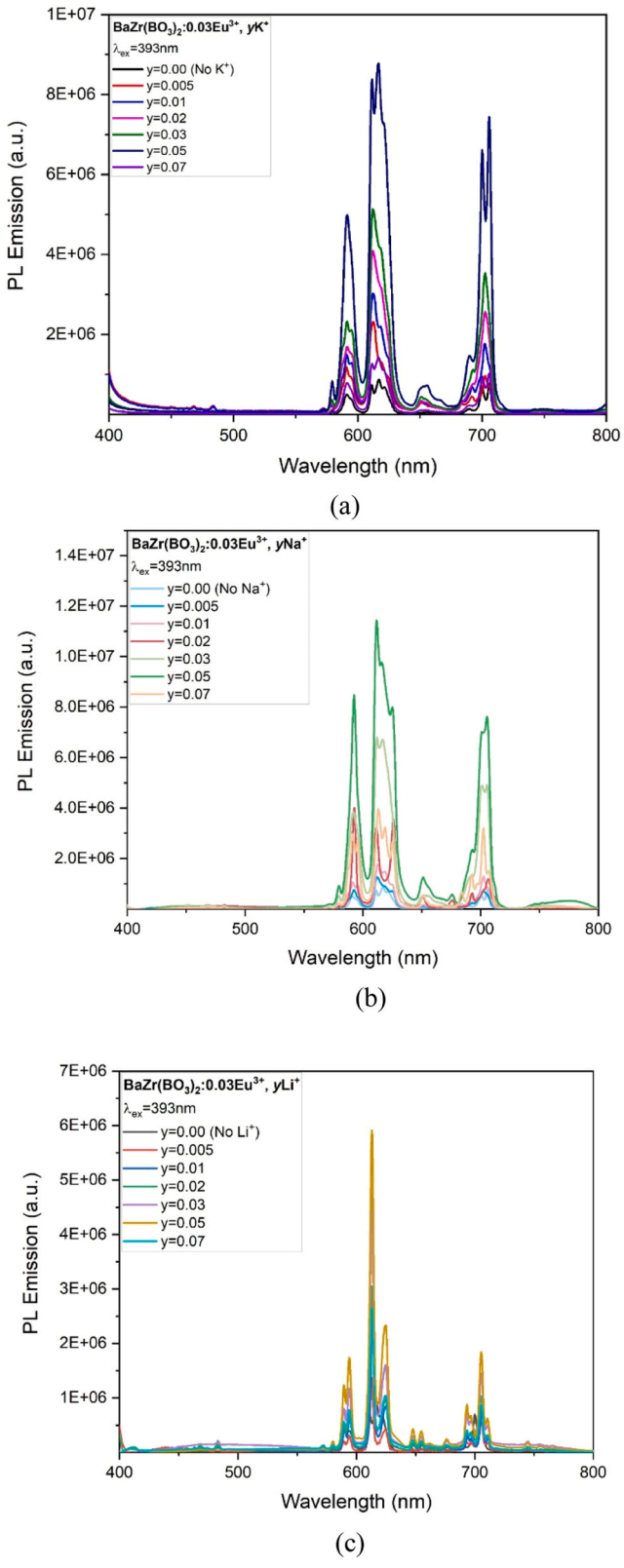

Fig. 6. Photoluminescence emission spectra of $BaZr(BO_3)_2$:0.03Eu^{3+} phosphors co-doped with different alkali ions under 393 nm excitation: (a) K^+, (b) Na^+, and (c) Li^+, showing the effect of co-dopant type and concentration on emission intensity.

Table 3
Representative effects of Li^+/Na^+/K^+ in Eu^{3+} phosphors.

Co-dopant	Typical effect on PL intensity	Typical structural role	Cite
Li^+	From weak to very strong enhancement; can strongly distort the local symmetry	Often interstitial or highly mismatched; may introduce vacancies/ distortion	[13,22, 70,72]
Na^+	Frequently gives strongest, most balanced enhancement	Good radius match with alkaline-earth/alkali sites; efficient charge compensation	[18,19, 21,26, 71]
K^+	Moderate enhancement; may be limited at high concentrations.	Larger radius; can induce strain/secondary phases	[22, 68–70]

suitable ionic radius and better compatibility with the host lattice, which facilitates effective charge compensation of Eu^{3+} substitution and reduces defect-related non-radiative recombination centers [74]. In contrast, the smaller Li^+ ion may induce stronger local lattice distortion and asymmetry around Eu^{3+} ions, while the larger K^+ ion may introduce comparatively higher lattice strain at elevated concentrations, both of which can limit emission enhancement.

The enhancement in PL intensity upon alkali co-doping is primarily associated with effective charge compensation and the consequent suppression of defect-assisted non-radiative relaxation pathways [75]. In addition, alkali co-doping may increase the local asymmetry and Eu–O covalency around Eu^{3+} ions, thereby enhancing the electric-dipole $^5D_0 \rightarrow {}^7F_2$ transition, which is consistent with the increased Ω_2 values obtained from Judd–Ofelt analysis [76]. At higher alkali concentrations, however, excessive lattice distortion and defect formation may lead to concentration quenching and to decreased emission intensity.

Furthermore, the improved defect regulation induced by alkali-ion co-doping is expected to contribute to enhanced thermal stability by suppressing thermally activated non-radiative processes, consistent with the temperature-dependent PL and activation energy results discussed in Section 3.7. Among the investigated alkali ions, Na^+ provides the most favorable balance between charge compensation, local symmetry modification, defect suppression, and lattice compatibility, leading to the optimum luminescence and thermal performance.

The superior performance of Na^+ can be attributed to its more suitable ionic radius and better compatibility with the host lattice, which facilitates effective charge compensation of Eu^{3+} substitution and reduces defect-related non-radiative recombination centers. In contrast, the smaller Li^+ ion may introduce local lattice distortion or occupy interstitial sites, while the larger K^+ ion may induce excessive lattice strain at higher concentrations, both of which can limit emission enhancement.

The enhancement in PL intensity upon alkali co-doping is primarily attributed to effective charge compensation and the consequent suppression of defect-related non-radiative recombination centers. This behavior indicates that alkali co-doping improves radiative efficiency by minimizing defect-assisted quenching pathways, particularly those associated with cation vacancies and oxygen-related defects. In addition, alkali co-doping may increase the local asymmetry and Eu–O covalency around Eu^{3+} ions, thereby enhancing the electric-dipole $^5D_0 \rightarrow {}^7F_2$ transition, which is expected to be reflected in higher Ω_2 values in the subsequent Judd–Ofelt analysis. In Eu^{3+}-activated phosphors, the intensity ratio between the electric-dipole $^5D_0 \rightarrow {}^7F_2$ transition (~612 nm) and the magnetic-dipole $^5D_0 \rightarrow {}^7F_1$ transition (~594 nm), expressed as I_{612}/I_{594}, is widely recognized as a sensitive indicator of local structural asymmetry around Eu^{3+} ions. For the Li^+-co-doped samples, this ratio increases from 3.38 to 4.41 with increasing Li^+ concentration, further confirming that Li^+ incorporation enhances the local asymmetry and crystal-field perturbation around Eu^{3+} ions. This trend is fully consistent with the increased Ω_2 values obtained from Judd–Ofelt analysis, further confirming that Li^+ incorporation enhances local

structural asymmetry and Eu–O covalency around Eu^{3+} ions, in agreement with recent reports on Eu^{3+}-activated phosphors. This correlation between enhanced $^5D_0 \rightarrow {}^7F_2$ intensity and reduced local symmetry is in good agreement with recent Eu^{3+} structural–luminescence studies in borotellurate and garnet hosts, where local coordination distortion and symmetry breaking were shown to strongly promote electric-dipole Eu^{3+} emission [77,78]. At higher alkali concentrations, however, the formation of additional defects or clustering effects may lead to concentration quenching, resulting in decreased emission intensity. Furthermore, this defect-suppression mechanism is expected to enhance the thermal stability of the phosphor by reducing thermally activated non-radiative pathways, which will be verified by the temperature-dependent photoluminescence and activation energy analysis presented in Section 3.6.

These results demonstrate that alkali co-doping is an effective strategy for tuning the luminescence performance of $BaZr(BO_3)_2$:Eu^{3+} phosphors, with Na^+ providing the most favorable balance between charge compensation and lattice compatibility. The observed trends are consistent with previous reports on alkali-assisted enhancement in rare-earth-doped borate and oxide phosphors. These results are consistent with the charge-compensation and defect-control strategy outlined in the introduction, confirming that alkali co-doping effectively suppresses non-radiative pathways and enhances radiative recombination efficiency in Eu^{3+}-activated phosphors.

3.7. Thermal stability, thermal quenching mechanism, and activation energy

The temperature-dependent photoluminescence (PL) spectra of $BaZr(BO_3)_2$:3 wt%Eu^{3+} and alkali co-doped samples (K^+, Li^+, and Na^+) were systematically recorded over the temperature range of 300–550 K under 393 nm excitation, as depicted in Fig. 7(a–e). For the 3 wt% Eu^{3+}-doped sample (Fig. 7a), the corresponding normalized emission profiles (Fig. 7e) reveal that the characteristic Eu^{3+} transitions ($^5D_0 \rightarrow {}^7F_J$, J = 0–4) are preserved over the entire temperature range, indicating that heating does not modify the underlying emission mechanism but mainly reduces the overall emission intensity.

With increasing temperature, a gradual decrease in PL intensity is observed for all samples, which is attributed to thermally activated non-radiative relaxation processes. In the undoped sample, a pronounced thermal quenching behaviour is observed above ~390 K, as shown in Fig. 7**e**. The effect of alkali co-doping on thermal stability can be directly compared from the normalized PL intensity retention curves shown in Fig. 7(e). For the K^+ co-doped sample (Fig. 7 **b**), the emission intensity shows improved retention at elevated temperatures compared to the undoped sample. A similar trend is observed for Li^+ co-doping (Fig. 7 **(c)**, although the improvement is relatively limited.

In contrast, the Na^+ co-doped sample (Fig. 7 **(d)** exhibits the highest thermal-intensity retention among the investigated samples. These results indicate that Na^+ co-doping provides comparatively improved thermal stability within the investigated alkali-ion series. In addition, a noticeable sharpening of the emission lines is observed for Li^+ and particularly Na^+ co-doped samples (Fig. 7(d–e)), which can be attributed to a more uniform local environment around Eu^{3+} ions and reduced inhomogeneous broadening resulting from improved lattice ordering and defect suppression.

The observed improvement in thermal stability upon alkali co-doping is likely associated with charge compensation effects and reduced defect-assisted non-radiative relaxation. The incorporation of monovalent ions (Li^+, Na^+, K^+) may reduce the concentration of cation vacancies and oxygen-related defects that act as non-radiative recombination centers. Consequently, thermally activated energy migration to these quenching centers is suppressed, resulting in improved emission stability. This suppression of energy migration to defect centers is known to increase the activation energy for thermal quenching and leads to a more gradual decrease in PL intensity with temperature, consistent with the flatter I(T) curves observed for alkali co-doped samples. It is also noted that the relative intensity of the $^5D_0 \rightarrow {}^7F_4$ transition (~702 nm) is more pronounced in the Eu^{3+} doped and K^+ co-doped samples (Fig. 7 **(a, b)**), whereas it decreases in Li^+ and Na^+ co-doped samples (Fig. 7 **(c,d)**).

This behavior suggests that alkali co-doping modifies not only the crystal field around Eu^{3+} ions but also their site distribution and local coordination, leading to changes in the relative intensity of the $^5D_0 \rightarrow {}^7F_4$ transition through combined effects of crystal field strength and Stark splitting [25,57]. Furthermore, alkali co-doping increases local asymmetry and Eu–O covalency, enhancing the electric-dipole $^5D_0 \rightarrow {}^7F_2$ transition and reducing thermal quenching, which is consistent with the increased emission intensity and higher Judd–Ofelt Ω_2 values [18,21].

In particular, the more clearly resolved Stark splitting of the $^5D_0 \rightarrow {}^7F_2$ transition in the Na^+ co-doped sample (Fig. 7**e**) indicates a stronger crystal field interaction and lower site symmetry, which further supports the presence of a more asymmetric and well-defined local environment around Eu^{3+} ions [55]. This sharpening and improved resolution of Stark components is consistent with previous reports on Eu^{3+}-activated borates and perovskites, where enhanced local structural order and more well-defined Eu^{3+} site occupancy result in narrower $^5D_0 \rightarrow {}^7F_2$ emission lines and are typically correlated with higher Judd–Ofelt Ω_2 parameters [2,52].

To quantitatively compare the thermal stability of the investigated phosphors, the normalized PL intensities at 450 K were evaluated. The undoped $BaZr(BO_3)_2$:3 wt%Eu^{3+} sample retains approximately 13% of its initial room-temperature emission intensity at 450 K, whereas the K^+-, Li^+-, and Na^+-co-doped samples retain about 16%, 21%, and 36%, respectively. These results indicate that alkali-ion co-doping improves the thermal stability of the phosphor by suppressing thermally activated non-radiative relaxation pathways. Among the investigated co-dopants, Na^+ exhibits the highest thermal-intensity retention, which may be associated with a more favorable balance between charge compensation, lattice compatibility, and reduced defect-assisted non-radiative relaxation.

The distinct thermal quenching behavior observed for the Na^+- and K^+-co-doped samples can be rationalized in terms of alkali-related defect chemistry. Systematic studies on Eu^{3+} phosphors show that alkali co-doping modifies the defect landscape by reducing vacancy concentrations and limiting energy migration toward quenching centers, thereby suppressing defect-assisted non-radiative recombination [79]. In our system, Na^+ provides a more favorable balance of charge compensation and lattice compatibility, which enables more efficient defect suppression than K^+, consistent with reports that Na^+ co-doping yields the most balanced enhancement of luminescence and thermal performance among Li^+/Na^+/K^+ series in Eu^{3+}-activated borates and related hosts [22]. Therefore, the improved thermal stability of the Na^+-co-doped composition is tentatively attributed to more effective suppression of vacancy-type defects (e.g., oxygen or cation vacancies) and a reduced probability of non-radiative relaxation at elevated temperatures.

The improved thermal stability plays a critical role in enabling practical solid-state lighting applications. A detailed investigation of the thermal quenching mechanism and activation energy is discussed in the subsequent section.

To quantitatively evaluate the thermal quenching behavior, the activation energy (E_a) was estimated using the Arrhenius equation:

$$\ln[(I_0/I) - 1] = \ln A - E_a/(kT) \quad (5)$$

where I_o and I are the emission intensities at room temperature and at temperature T, respectively, k is the Boltzmann constant, and A is a constant. The plots of $\ln[(I_o/I) - 1]$ versus $1/kT$ for $BaZr(BO_3)_2$:3 wt% Eu^{3+} and alkali co-doped samples are shown in Fig. 8**(a–d)**. The activation energy was determined from the slope of the linear fitting. The obtained slopes are −0.523, −0.398, −0.258, and −0.264 for the Eu^{3+}-only, K^+, Li^+, and Na^+ co-doped samples, respectively, corresponding to activation energies of approximately 0.52, 0.40, 0.26, and 0.26 eV.

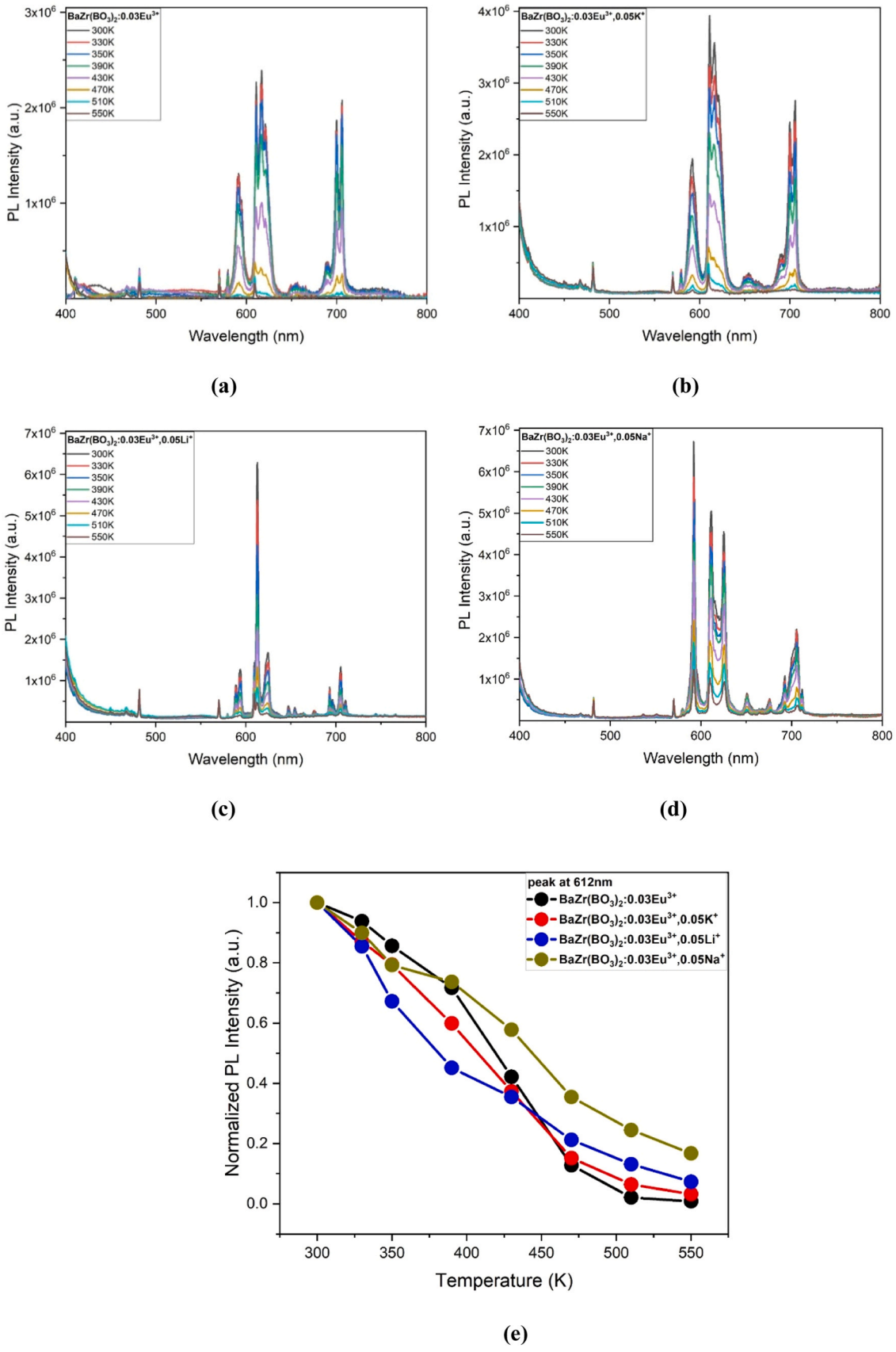

Fig. 7. Temperature-dependent photoluminescence (PL) spectra and normalized emission intensity of $BaZr(BO_3)_2$:0.03Eu^{3+} and alkali co-doped samples under 393 nm excitation: (a) $BaZr(BO_3)_2$:0.03Eu^{3+}, (b) $BaZr(BO_3)_2$:0.03Eu^{3+},0.05 K^+, (c) $BaZr(BO_3)_2$:0.03Eu^{3+},0.05Li^+, and (d) $BaZr(BO_3)_2$:0.03Eu^{3+},0.05Na^+. (e) Comparative normalized PL intensity retention curves of all samples as a function of temperature, monitored at 612 nm.

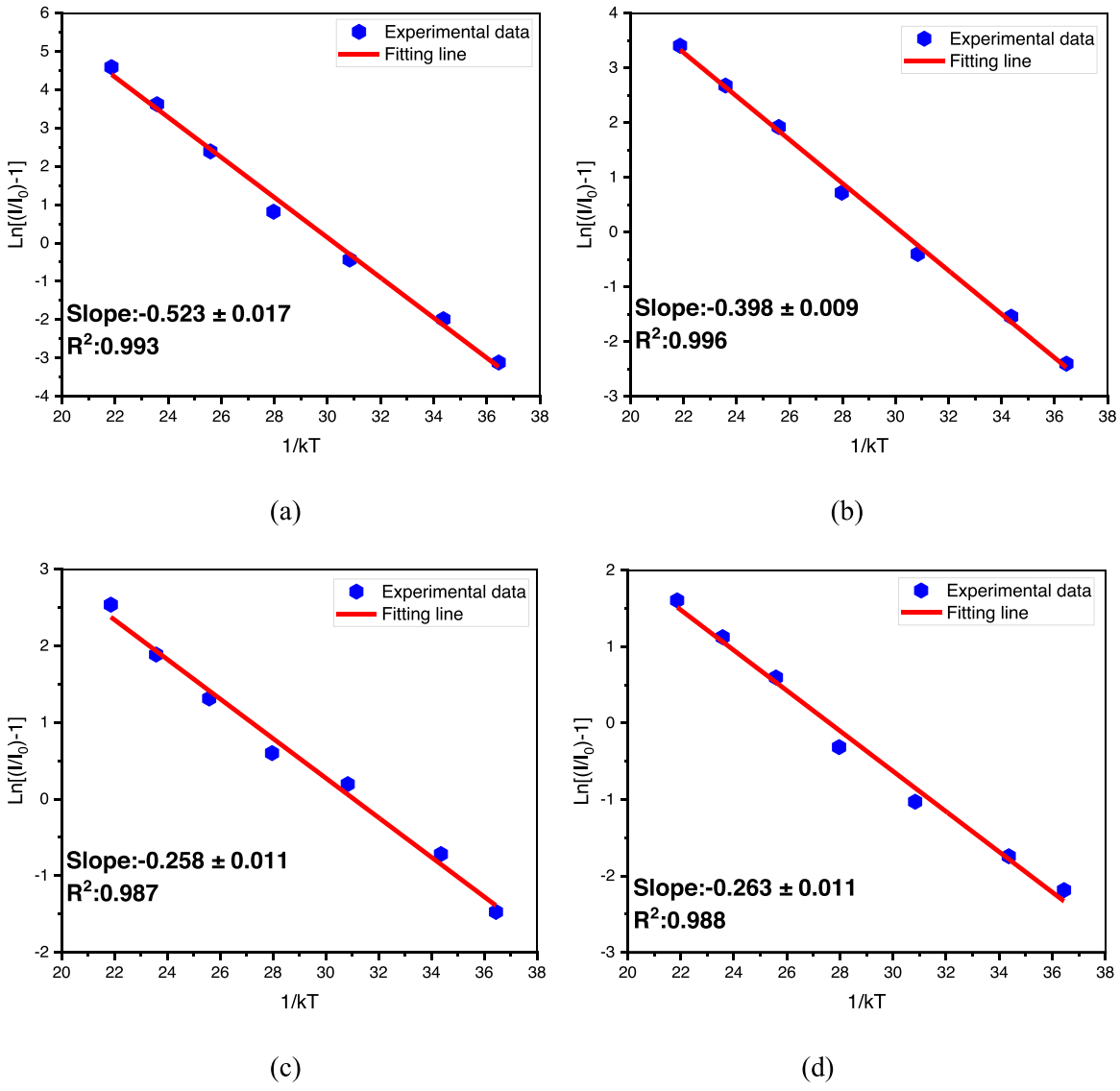

Fig. 8. Temperature dependent Arrhenius plots of $\ln[(I_0/I) - 1]$ as a function of 1/kT for (a) $BaZr(BO_3)_2$:3 wt%Eu^{3+}, (b) 5 wt% K^+ co-doped, (c) 5 wt% Li^+ co-doped, and (d) 5 wt% Na^+ co-doped samples.

The Eu^{3+}-only sample exhibits the highest activation energy; however, it shows the most pronounced thermal quenching behavior. In contrast, alkali co-doped samples display lower activation energies but significantly improved thermal stability, indicating that activation energy alone does not fully govern thermal quenching behavior.

This apparent discrepancy can be explained by considering defect-assisted non-radiative relaxation pathways. Alkali co-doping modifies the defect landscape by reducing vacancy concentrations and limiting energy migration toward quenching centers. As a result, even with slightly lower activation energies, the co-doped samples exhibit improved thermal stability due to reduced non-radiative recombination probability.

Among the co-doped samples, Na^+ and Li^+ exhibit similar activation energies (~0.26 eV), while K^+ shows a moderately higher value (~0.40 eV). Despite this, Na^+ co-doping demonstrates the best thermal stability, suggesting that efficient defect suppression and improved local structural ordering play a more dominant role than activation energy alone. The superior performance of Na^+ co-doping can be attributed to its favorable ionic radius and better lattice compatibility, which enables more efficient defect compensation compared to Li^+ and K^+. Similar behavior has been reported in Eu^{3+}-activated borate and perovskite systems, where Na^+ co-doping leads to enhanced thermal stability due to improved local structural ordering and more effective suppression of non-radiative centers [20,72].

These results confirm that alkali co-doping enhances thermal stability primarily through defect control and suppression of non-radiative pathways, rather than solely increasing the activation energy barrier. This behavior is consistent with previous studies on Eu^{3+}-activated phosphors, where activation energy is not always the sole factor governing thermal stability. In many oxide and borate hosts, thermal quenching has been shown to strongly depend on non-radiative pathways associated with defects and energy migration processes [56,70,72]. In particular, Eu^{3+} substitution into divalent cation sites often introduces charge imbalance and cation vacancies, which act as non-radiative recombination centers [72].

Alkali co-doping (Li^+, Na^+, K^+) has been widely reported to effectively compensate this charge imbalance, suppress defect-related quenching centers, and consequently improve both luminescence intensity and thermal stability [80,81]. In such systems, the improvement in thermal performance is primarily attributed to defect control and reduced energy migration to quenching centers, rather than solely to an increase in activation energy [82].

More specifically, similar behavior has been reported in Eu^{3+}-activated phosphors with alkali co-doping. In $SrLaNaTeO_6:Eu^{3+},M^+$ systems, $Li^+/Na^+/K^+$ co-doping effectively compensates the charge imbalance arising from $Eu^{3+} \rightarrow Sr^{2+}$ substitution, thereby suppressing defect-related quenching, with Na^+ providing the best performance due to its optimal ionic radius matching with Sr^{2+} [72]. A similar "self-compatible Na^+" effect has also been reported in $Na_{13}Sr_2Ta_2(PO_4)_9:Eu^{3+},A^+$ phosphors, where Na^+ co-doping leads to superior luminescence performance [20].

In addition, studies on $GdPO_4:Eu^{3+},A^+$ systems have shown that the choice of alkali ion significantly influences both emission intensity and thermal stability through its impact on local structure and defect chemistry [73]. Likewise, in $K_3Y(BO_2)_6:Eu^{3+},Li^+/Na^+$ phosphors, alkali co-doping has been reported to enhance both activation energy and thermal stability, further confirming the crucial role of defect compensation and local structural modification in controlling thermal quenching behaviour [70].

3.8. Comparative performance analysis with previously reported Eu3 + -activated red phosphors

To further evaluate the luminescence performance and application potential of the present $BaZr(BO_3)_2:Eu^{3+},A^+$ (A = Li^+, Na^+, K^+) phosphors, a comparative analysis with representative Eu^{3+}-activated red phosphors previously reported for near-UV excited WLED/pc-WLED applications was carried out, as summarized in Table 4. Recent studies have demonstrated that Eu^{3+}-activated borate- and oxide-based phosphors can exhibit excellent color purity, high quantum efficiency, and remarkable thermal stability through various structural engineering approaches, including alkali-ion co-doping, energy-transfer regulation, concentration-quenching suppression, and local symmetry distortion. For example, $LaSc_3(BO_3)_4:Eu^{3+}$ phosphors exhibited zero-thermal-quenching behavior with a high quantum efficiency of 88.3%, while $Gd(BO_2)_3–Y_3BO_6–GdBO_3:Eu^{3+}$ phosphors achieved an exceptionally high color purity of 99.5%. Similarly, $Ba_3Lu_2B_6O_{15}:Eu^{3+}$ phosphors retained nearly 98% of their room-temperature emission intensity at 450 K due to one-dimensional structural confinement.

Compared with these studies, the present $BaZr(BO_3)_2:Eu^{3+},A^+$ phosphors provide a distinct advantage in terms of systematic alkali-assisted luminescence engineering and comprehensive structure–property correlation analysis. In particular, the simultaneous comparison of Li^+, Na^+, and K^+ co-doping effects within the same host lattice reveals the critical role of alkali-ion radius and charge compensation in regulating local symmetry, Eu–O covalency, defect formation, and non-radiative relaxation pathways. Among the investigated samples, Na+ co-doping resulted in the most balanced luminescence performance, yielding approximately 12-fold emission enhancement together with improved thermal stability and favorable chromaticity characteristics. Furthermore, the combined use of Judd–Ofelt analysis, TRPL measurements, and thermal quenching analysis provides deeper insight into the relationship between defect suppression and radiative efficiency, demonstrating that thermal stability is governed not only by activation energy but also by the reduction of defect-assisted non-radiative recombination pathways.

Although several previously reported Eu^{3+}-activated red phosphors exhibit higher color purity or quantum efficiency values, the present $BaZr(BO_3)_2:Eu^{3+},A+$ phosphors provide a more comprehensive mechanistic understanding of alkali-assisted luminescence enhancement in borate hosts. In particular, this work presents a systematically benchmarked alkali-series study within a single host lattice combined with Judd–Ofelt analysis, TRPL characterization, and thermal quenching analysis. This comprehensive approach enables direct correlation between alkali-ion radius, Eu–O covalency, defect chemistry, and radiative/non-radiative relaxation dynamics, demonstrating that alkali-ion charge compensation is an effective strategy for simultaneously

Table 4
Comparison of photoluminescence performance, quantum efficiency, and thermal stability parameters of representative Eu3 + -activated red phosphors reported for near-UV excited WLED applications.

No.	Phosphor Composition	Excitation (nm)	Main Emission (nm)	Color Purity (%)	IQE/QE (%)	Thermal Stability	Special Feature / Mechanism	Ref.
1	$K_7SrY_2(B_5O_{10})_3:Eu^{3+},Li^+$	394	612	97.7	—	Ea = 0.190 eV	Li^+-induced local symmetry distortion and enhanced Ω_2	[25]
2	$LiCaY_5(BO_3)_6:Eu^{3+}$, Tb^{3+}	231 / UV-NUV	Red & Green	—	—	Good thermal behavior	$Tb^{3+} \rightarrow Eu^{3+}$ energy transfer and tunable emission	[83]
3	$Ca_3Y(AlO_3)(BO_3)_4:Eu^{3+}$	397	621	90	88	76.3% at 150 °C	High-efficiency thermally stable red phosphor	[84]
4	$Ba_5P_6O_{20}:Eu^{3+},A^+$ (Li^+/Na^+/K^+)	393	612	—	37.5	93.5% at 423 K	Alkali charge compensation improves PL and thermostability	[18]
5	$K_3Y(BO_2)_6:Eu^{3+},Li^+/Na^+$	612 excitation emission system	612	—	—	Ea = 0.1389–0.2536 eV	Alkali-enhanced PL and abnormal thermal stability	[70]
6	$GdAl_3(BO_3)_4:Dy^{3+},Eu^{3+}$	UV	Visible region	—	ET efficiency 84%	—	$Dy^{3+} \rightarrow Eu^{3+}$ energy transfer	[85]
7	$LaMgB_5O_{10}:Eu^{3+},A^+$	—	Far-red enhanced	—	—	Anti-thermal quenching	Alkali-induced redistribution of oscillator strength	[56]
8	$Ba_3Lu_2B_6O_{15}:Eu^{3+}$	398	593	97.5	~53	~98% intensity retained at 450 K	One-dimensional structural confinement suppresses concentration quenching	[86]
9	$Li_3Y_3BaSr(MoO_4)_8:Sm^{3+},Eu^{3+}$	NUV / Blue	Deep red (645)	88.5	—	87% retained at 400 K	Narrow-band deep-red emission for plant growth LEDs	[87]
10	$Gd(BO_2)_3–Y_3BO_6–GdBO_3:Eu^{3+}$	394	612	99.5	58.4	Ea = 0.319 eV	Heavy Eu^{3+} doping with excellent color purity	[88]
11	$Na_3Y(BO_3)_2:Tb^{3+},Eu^{3+}$	395	Red emission	84.7	83.5	95% retained at 450 K	Efficient $Tb^{3+} \rightarrow Eu^{3+}$ ET and narrow-band red emission	[89]
12	$Ba_3Lu_4O_9:Eu^{3+}$	396	614	98	82	64% retained at 423 K	High color purity and high QE warm-WLED phosphor	[90]
13	$BaZr(BO_3)_2:Eu^{3+},Li^+/Na^+/K^+$	393	612	Up to 86	—	Improved thermal stability via defect suppression	Systematic alkali-dependent charge compensation, JO analysis, TRPL, and defect-assisted thermal quenching mechanism	*This work*

tuning emission intensity, local asymmetry, radiative dynamics, and thermal robustness in near-UV-excited red phosphors.

3.9. Photoluminescence decay and lifetime analysis

Time-resolved photoluminescence decay curves of $BaZr(BO_3)_2$:Eu^{3+} and alkali co-doped samples were obtained under 393 nm excitation (Fig. 9), revealing non-single-exponential behavior that was well described by a bi-exponential fitting function:

$$I(t) = A_1 \exp\left(-\frac{t}{\tau_1}\right) + A_2 \exp\left(-\frac{t}{\tau_2}\right) \quad (6)$$

where τ_1 and τ_2 correspond to the fast and slow decay components, respectively, and A_1 and A_2 represent their relative contributions. The average lifetime (τ_{avg}) was calculated using:

$$\tau_{avg} = \frac{A_1\tau_1^2 + A_2\tau_2^2}{A_1\tau_1 + A_2\tau_2} \quad (7)$$

The fitted parameters and calculated average lifetimes are summarized in Table 5. The obtained χ^2 values (~1.13–1.22) indicate excellent agreement between the experimental decay profiles and the bi-exponential fitting model, confirming the reliability of the lifetime analysis.

The obtained lifetimes are 1.714 ms for $BaZr(BO_3)_2$:0.01Eu^{3+}, 1.785 ms for 0.03Eu^{3+}, 2.263 ms for K^+ co-doped, 1.637 ms for Li^+ co-doped, and 1.927 ms for Na^+ co-doped samples. These values fall within the typical range reported for Eu^{3+}-activated borate phosphors and are in good agreement with previously reported lifetimes (1.35–1.82 ms) for $BaZr(BO_3)_2$:Eu^{3+} systems [12].

The presence of bi-exponential decay behavior suggests that Eu^{3+} ions occupy slightly different local environments or are influenced by defect-related energy transfer processes. The fast decay component (τ_1) is generally attributed to defect-assisted non-radiative relaxation processes, whereas the slow component (τ_2) corresponds to intrinsic radiative recombination of Eu^{3+} ions.

A clear dependence of lifetime on alkali co-doping is observed. The K^+-co-doped sample exhibits the longest lifetime (2.263 ms), indicating a suppression of non-radiative decay pathways and improved radiative efficiency. In contrast, the Li^+-co-doped sample shows a shorter lifetime (1.637 ms) despite exhibiting a high asymmetry ratio and enhanced electric-dipole transition probability. This behavior suggests that while Li^+ incorporation strongly distorts the local environment and enhances radiative transitions, it may simultaneously introduce lattice defects or energy transfer channels that increase non-radiative relaxation.

The Na^+-co-doped sample exhibits intermediate behavior, indicating a balance between structural distortion and defect formation. The relatively small variation in lifetimes among the samples confirms that the primary emission mechanism remains unchanged, while the efficiency is governed by the competition between radiative and non-radiative processes.

These results are fully consistent with the Judd–Ofelt analysis presented in Section 3.11. In particular, the K^+-co-doped sample, which shows moderate Ω_2 values, exhibits the longest lifetime, indicating reduced non-radiative losses. Conversely, the Li^+-co-doped sample, characterized by a significantly enhanced Ω_2 parameter, shows a shorter lifetime, highlighting that increased local asymmetry does not necessarily lead to improved luminescence efficiency. This demonstrates that an optimal balance between symmetry breaking and defect suppression is essential for achieving high-performance Eu^{3+}-activated phosphors. These findings further confirm that the luminescence performance is governed by the competition between radiative and non-radiative processes, where defect suppression plays a more critical role than local symmetry enhancement alone.

3.10. Chromaticity coordinates and color purity evaluation

The emission-derived chromaticity coordinates of $BaZr(BO_3)_2$:Eu^{3+} phosphors with different Eu^{3+} concentrations and alkali co-doping levels were projected onto the CIE 1931 color space (Fig. 10 **(a–d)**). The calculated *x–y* coordinates, correlated color temperature (CCT), and color purity (CP) values are presented in Table 6.

As listed in Table 6, all samples exhibit chromaticity coordinates located in the red region ($x \approx 0.53–0.63$, $y \approx 0.28–0.35$), confirming that the emission is dominated by the hypersensitive $^5D_0 \rightarrow {}^7F_2$ transition of Eu^{3+} ions. The Eu^{3+} concentration series shows a slight shift in chromaticity coordinates with increasing dopant content, while the color purity varies from 60% to 81%, reaching a maximum at higher Eu^{3+} concentrations. This indicates that concentration tuning can enhance emission purity without significantly altering the emission color.

For the K^+ co-doped compositions, the CIE chromaticity coordinates exhibit a broader dispersion (x ≈ 0.47–0.62, y ≈ 0.28–0.34), together with a marked enhancement in color purity from 41% to 85% as the K^+ content increases. This systematic evolution evidences that K^+

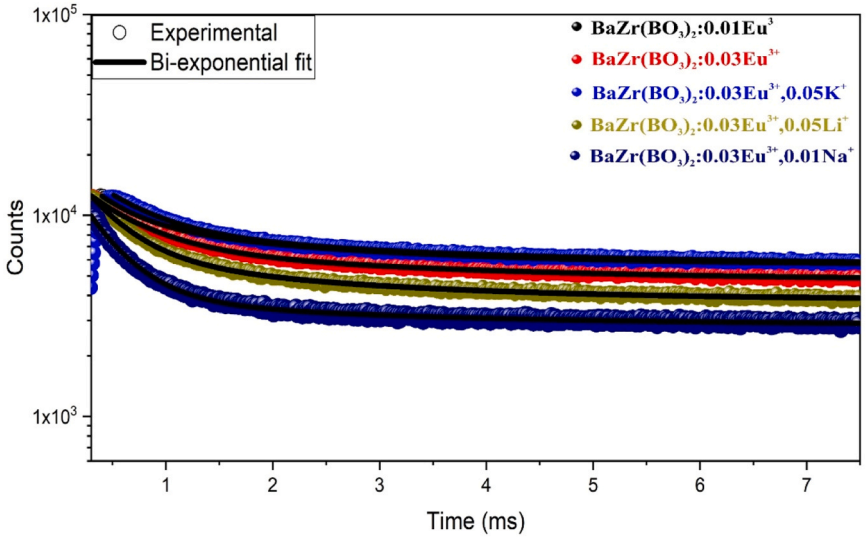

Fig. 9. Photoluminescence decay curves of $BaZr(BO_3)_2$:Eu^{3+} and alkali co-doped samples monitored at 612 nm under 393 nm excitation. Open circles represent the experimental decay data, while the solid lines correspond to the bi-exponential fitting curves.

Table 5
Decay parameters of $BaZr(BO_3)_2:Eu^{3+}$ and alkali co-doped samples obtained from bi-exponential fitting of photoluminescence decay curves. The fast (τ_1) and slow (τ_2) components, their relative contributions (Rel.%), average lifetime (τ_{avg}), and fitting quality (χ^2) are listed.

		Time(μs)	Rel.%	τ_{avg}(ms)	χ^2
$BaZr(BO_3)_2:0.01Eu^{3+}$	τ_1	33.588 ± 0.034	19.49 ± 0.02	1.714 ± 0.002	1.1597 ± 0.003
	τ_2	1754.862 ± 1.755	80.51 ± 0.08		
$BaZr(BO_3)_2:0.03Eu^{3+}$	τ_1	451.412 ± 0.451	33.58 ± 0.03	1.785 ± 0.007	1.1664 ± 0.004
	τ_2	2459.940 ± 2.460	66.42 ± 0.07		
$BaZr(BO_3)_2:0.03Eu^{3+},0.05\ K^{+}$	τ_1	449.212 ± 0.449	27.65 ± 0.03	2.263 ± 0.009	1.1309 ± 0.002
	τ_2	2403.156 ± 2.403	72.35 ± 0.07		
$BaZr(BO_3)_2:0.03Eu^{3+},0.05Li^{+}$	τ_1	32.873 ± 0.033	34.56 ± 0.03	1.637 ± 0.002	1.1377 ± 0.002
	τ_2	1722.868 ± 1.723	65.44 ± 0.07		
$BaZr(BO_3)_2:0.03Eu^{3+},0.05Na^{+}$	τ_1	29.984 ± 0.030	58.84 ± 0.06	1.927 ± 0.004	1.2186 ± 0.005
	τ_2	2033.622 ± 2.034	41.16 ± 0.04		

incorporation is highly effective in optimizing the red-emission characteristics, primarily through the suppression of non-radiative recombination channels and the concomitant promotion of radiative transition probability. The proposed mechanism is corroborated by photoluminescence decay analyses, which reveal noticeably prolonged excited-state lifetimes in the K^+ co-doped samples, thereby confirming that K^+ co-doping not only boosts the emission intensity but also improves the overall optical robustness of the phosphor.

In contrast, the Li^+-co-doped samples show moderate fluctuations in chromaticity coordinates ($x \approx 0.43–0.61$, $y \approx 0.29–0.35$) and color purity values ranging from 31% to 81%. The relatively lower color purity at low Li^+ concentrations may be attributed to increased structural distortion and defect formation, which can affect emission uniformity. However, at higher Li^+ concentrations, the color purity improves, indicating a partial stabilization of the emission process.

The Na^+-co-doped samples exhibit relatively stable chromaticity coordinates ($x \approx 0.51–0.63$, $y \approx 0.28–0.35$) with consistently high color purity values (55%–86%). Notably, the highest color purity (~86%) is achieved at intermediate Na^+ concentrations, suggesting an optimal balance between local symmetry modification and defect suppression.

The correlated color temperature (CCT) values listed in Table 6 fall within the range of ~1600–2200 K, indicating warm red emission suitable for solid-state lighting and display applications. The observed variations in chromaticity coordinates and color purity are consistent with the Judd–Ofelt analysis, where changes in the Ω_2 parameter reflect modifications in local asymmetry and electric-dipole transition probability.

The variations observed in the chromaticity coordinates among different samples are mainly associated with changes in the local crystal-field environment and symmetry around Eu^{3+} ions induced by alkali co-doping and concentration-dependent structural distortion. Different alkali ions (Li^+, Na^+, and K^+) produce different degrees of charge compensation, local asymmetry, and defect regulation, thereby modifying the relative intensities of the Eu^{3+} magnetic-dipole ($^5D_0 \rightarrow {}^7F_1$) and electric-dipole ($^5D_0 \rightarrow {}^7F_2$) transitions [91]. Since the hypersensitive $^5D_0 \rightarrow {}^7F_2$ transition strongly depends on the local symmetry and Eu–O covalency around Eu^{3+} ions, even moderate changes in lattice distortion and crystal-field strength can result in noticeable shifts in the calculated CIE chromaticity coordinates [91,92].

In addition, variations in Eu^{3+} concentration and alkali-ion content may alter the balance between radiative and non-radiative relaxation pathways, leading to changes in the relative emission-band intensities rather than fundamentally different emission colors [93]. Therefore, the observed chromaticity-coordinate shifts are attributed to systematic modifications of local symmetry, crystal-field strength, and defect populations around Eu^{3+} ions caused by alkali-ion incorporation [91,92].

Overall, the results demonstrate that both Eu^{3+} concentration and alkali co-doping enable fine tuning of emission color, color purity, and thermal characteristics without significantly altering the dominant red emission, highlighting the potential of $BaZr(BO_3)_2:Eu^{3+}$ phosphors for optoelectronic applications.

3.11. Judd–Ofelt analysis and radiative properties of Eu^{3+} emission

To quantitatively evaluate the radiative properties and local coordination environment of Eu^{3+} ions in $BaZr(BO_3)_2$ and alkali co-doped samples, a modified Judd–Ofelt (J–O) analysis was performed based on the emission spectra [94,95]. In Eu^{3+}-activated systems, the $^5D_0 \rightarrow {}^7F_1$ transition is predominantly of magnetic-dipole (MD) character and is largely insensitive to the local crystal field, whereas the $^5D_0 \rightarrow {}^7F_2$ and $^5D_0 \rightarrow {}^7F_4$ transitions are electric-dipole (ED) allowed and strongly dependent on-site symmetry and covalency. Therefore, the $^5D_0 \rightarrow {}^7F_1$ transition was used as an internal reference for the determination of radiative parameters.

The spontaneous emission probability of the magnetic-dipole transition is expressed as:

$$A_{MD}\left({}^5D_0 \rightarrow {}^7F_1\right) = A_{MD}^{(0)} n^3 \tag{8}$$

where $A_{MD}^{(0)} = 14.65 s^{-1}$ is the spontaneous emission probability in vacuum and n is the refractive index of the host matrix. For the present borate system, $n = 1.75$ was adopted as a reasonable approximation.

The radiative transition probabilities for other transitions were determined relative to the magnetic-dipole transition using the experimentally integrated emission intensities:

$$A_{0J} = A_{01}\left(\frac{I_{0J}}{I_{01}}\right)\left(\frac{\nu_{01}}{\nu_{0J}}\right) \tag{9}$$

where $I_{0\,J}$ and I_{01} are the integrated emission intensities of the $^5D_0 \rightarrow {}^7F_J$ and $^5D_0 \rightarrow {}^7F_1$ transitions, respectively, and $\nu_{0\,J}$ is the corresponding transition energy (cm^{-1}). The experimental transition oscillator strengths were determined from the integrated emission intensities of the Eu^{3+} emission bands relative to the magnetic-dipole $^5D_0 \rightarrow {}^7F_1$ transition. The experimentally obtained transition probabilities were subsequently analyzed within the framework of Judd–Ofelt theory to determine the Ω_2 and Ω_4 intensity parameters. According to the Judd–Ofelt theory, the radiative transition probability for electric-dipole transitions can be expressed as [94,96,97]:

$$A_{0J} = \frac{64\pi^4 e^2 \nu^3}{3h(2J+1)} \chi_{ed} \Omega_\lambda \left|\langle {}^7F_1 || U^{(\lambda)} || {}^5D_0 \rangle\right|^2 \tag{10}$$

where e is the electron charge, h is Planck's constant, and Ω_λ (λ=2,4) are the Judd–Ofelt intensity parameters. The local field correction factor χ_{ed} is given by [98,99]:

$$\chi_{ed} = \frac{n(n^2+2)^2}{9} \tag{11}$$

The squared reduced matrix elements $\left|\langle {}^7F_1 || U^{(\lambda)} || {}^5D_0 \rangle\right|^2$ are host-independent constants taken from the literature. In the present emission-based analysis, Ω_2 and Ω_4 parameters were reliably determined from the $^5D_0 \rightarrow {}^7F_2$ and $^5D_0 \rightarrow {}^7F_4$ transitions, respectively, while Ω_6 was not evaluated due to the absence of a measurable $^5D_0 \rightarrow {}^7F_6$ transition.

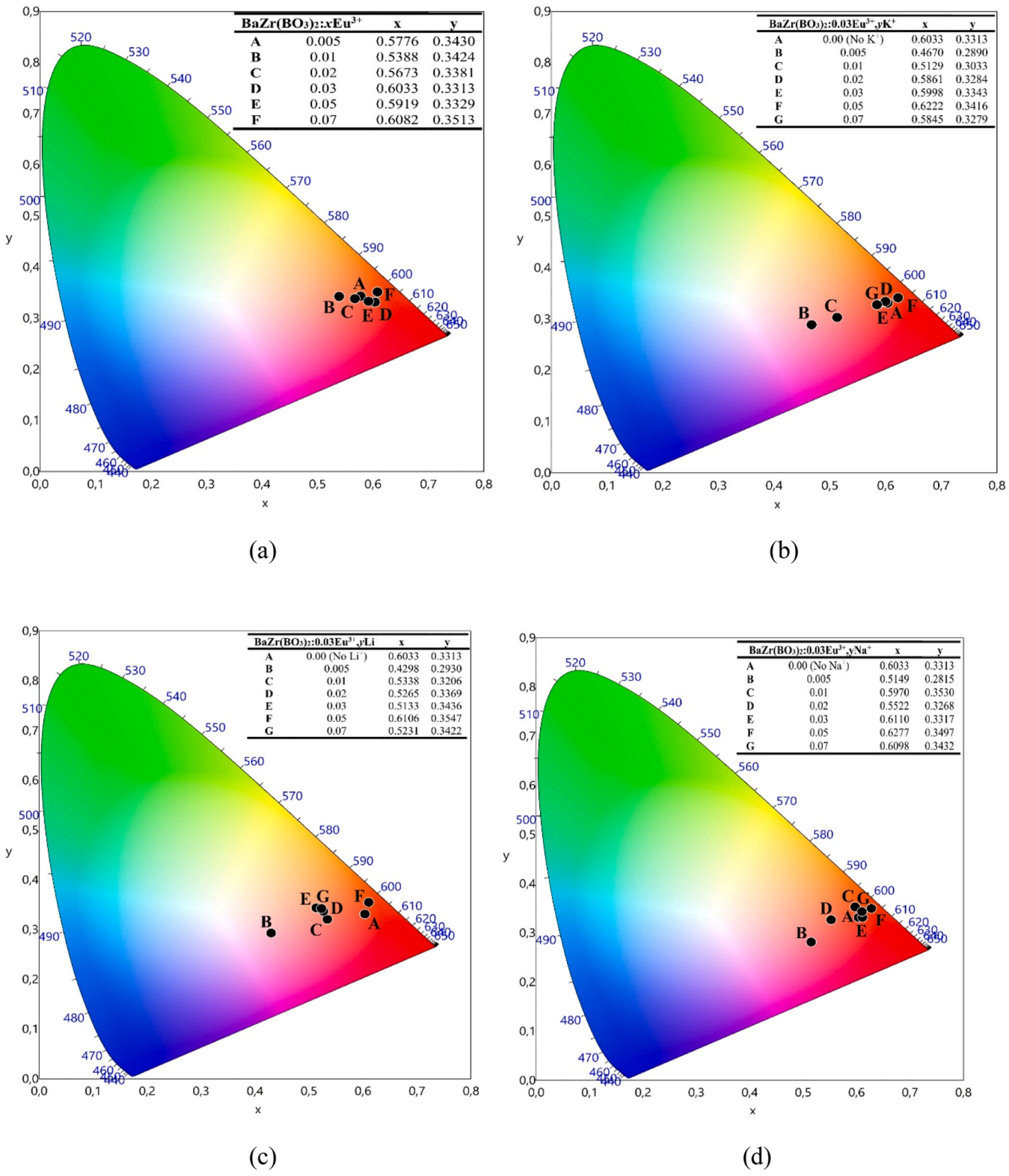

Fig. 10. CIE 1931 chromaticity diagrams of $BaZr(BO_3)_2:Eu^{3+}$ phosphors showing the effect of (a) Eu^{3+} concentration, (b) K^+ co-doping, (c) Li^+ co-doping, and (d) Na^+ co-doping on emission color coordinates.

Table 6
CIE 1931 chromaticity coordinates (*x*, *y*), correlated color temperature (CCT), and color purity (CP%) of $BaZr(BO_3)_2:Eu^{3+}$ phosphors as a function of Eu^{3+} concentration and alkali co-doping (K^+, Li^+, Na^+).

Eu^{3+} content (wt%)	*x*	*y*	CCT	Color Purity (CP)%
$x = 0.05$	0.5776	0.3430	1754	72
$x = 1$	0.5388	0.3424	1623	60
$x = 2$	0.5673	0.3381	1738	69
$x = 3$	0.6033	0.3313	2147	79
$x = 5$	0.5919	0.3329	1996	76
$x = 7$	0.6082	0.3513	1866	81
K^+ content (wt%)	*x*	*y*	CCT	Color Purity (CP)%
$y = 0.05$	0.4670	0.2890	1622	41
$y = 1$	0.5129	0.3033	1734	53
$y = 2$	0.5861	0.3284	2018	74
$y = 3$	0.5998	0.3343	2050	78
$y = 5$	0.6222	0.3416	2143	85
$y = 7$	0.5845	0.3279	2010	74
Li^+ content (wt%)	*x*	*y*	CCT	Color Purity (CP)%
$y = 0.5$	0.4298	0.2930	1886	31
$y = 1$	0.5338	0.3206	1701	59
$y = 2$	0.5265	0.3369	1620	57
$y = 3$	0.5133	0.3436	1652	53
$y = 5$	0.6106	0.3547	1843	81
$y = 7$	0.5231	0.3422	1626	56
Na^+ content (wt%)	*x*	*y*	CCT	Color Purity (CP)%
$y = 0.05$	0.5149	0.2815	2228	55
$y = 1$	0.5970	0.3530	1775	77
$y = 2$	0.5522	0.3268	1753	64
$y = 3$	0.6110	0.3317	2227	81
$y = 5$	0.6277	0.3497	2050	86
$y = 7$	0.6098	0.3432	1993	81

The total radiative transition probability is obtained by summing over all transitions:

$$A_{rad} = \sum_J A_{0J} \tag{12}$$

The branching ratio for each transition is defined as:

$$\beta_J = \frac{A_{0J}}{\sum_J A_{0J}} \tag{13}$$

The radiative lifetime of the $^5D_0$ level is given by:

$$\tau_{rad} = \frac{1}{A_{rad}} \tag{14}$$

By comparing the experimental lifetime (τ_{exp}) obtained from decay measurements with the calculated radiative lifetime, the internal quantum efficiency can be estimated as:

$$\eta = \frac{\tau_{exp}}{\tau_{rad}} \tag{15}$$

and the non-radiative decay rate is expressed as:

$$A_{nr} = \frac{1}{\tau_{exp}} - \frac{1}{\tau_{rad}} \tag{16}$$

In addition, the asymmetry ratio, which provides a direct measure of the local site symmetry around Eu^{3+}, is defined as:

$$R = \frac{I(^5D_0 \rightarrow {}^7F_2)}{^5D_0 \rightarrow {}^7F_1} \tag{17}$$

Table 7
Asymmetry ratios of Eu^{3+} emission transitions.

Sample	$I(^5D_0 \rightarrow {}^7F_1)$	$I(^5D_0 \rightarrow {}^7F_2)$	R
$BaZr(BO_3)_2:Eu^{3+}$	27.805	16.008	0.576
$+K^+$	32.025	23.830	0.744
$+Li^+$	22.597	154.779	6.849
$+Na^+$	27.653	28.381	1.026

Table 8
Radiative transition probabilities and Judd–Ofelt parameters.

Sample	$A(^5D_0 \rightarrow {}^7F_2)$ (s^{-1})	$A(^5D_0 \rightarrow {}^7F_4)$ (s^{-1})	Ω_2 ($\times 10^{-20}$ cm^2)	Ω_4 ($\times 10^{-20}$ cm^2)
Eu^{3+}	~45	~60	~2.1	~3.5
$+K^+$	~58	~62	~2.6	~3.6
$+Li^+$	~540	~85	~22.5	~4.8
$+Na^+$	~80	~68	~3.8	~3.9

A higher value of *R* indicates a lower symmetry and stronger covalent environment around Eu^{3+} ions.

The asymmetry ratio $R = I(^5D_0 \rightarrow {}^7F_2) / I(^5D_0 \rightarrow {}^7F_1)$, derived from the integrated emission intensities, provides a direct indication of the local site symmetry around Eu^{3+} ions. The calculated values are summarized in Table 7.

As shown in Table 7, the asymmetry ratio increases significantly upon alkali co-doping, reaching a maximum value in the Li^+-co-doped sample. This indicates a pronounced reduction in local symmetry and a strong enhancement of electric-dipole transitions. In contrast, Na^+ and K^+ co-doping result in moderate and relatively weak symmetry distortion, respectively. The observed variation in Ω_2 values among the alkali co-doped samples can be attributed to differences in ionic radius, local lattice distortion, and charge-compensation behavior induced by the alkali ions. Since Ω_2 is highly sensitive to the local asymmetry and covalency around Eu^{3+} ions, larger Ω_2 values indicate stronger crystal-field perturbation and lower local symmetry. In particular, Li^+ co-doping produces the highest Ω_2 value because the small ionic radius of Li^+ induces stronger local lattice distortion and modifies the Eu–O coordination environment more effectively than Na^+ and K^+ ions. This enhanced local asymmetry increases the electric-dipole character of the $^5D_0 \rightarrow {}^7F_2$ transition and strengthens Eu–O covalency. In contrast, K^+ ions, owing to their larger ionic radius, introduce comparatively weaker local crystal-field perturbation, resulting in relatively lower Ω_2 values. The intermediate Ω_2 behavior observed for Na^+ co-doping suggests a balanced interplay between local symmetry breaking, lattice compatibility, and defect suppression.

Using a refractive index of $n = 1.75$, the spontaneous emission probability of the magnetic-dipole transition was calculated as $A_{MD} = 78.5\ s^{-1}$. The radiative transition probabilities for the electric-dipole transitions were obtained from the integrated emission intensities and are summarized in Table 8. The Ω_6 parameter was not evaluated in the present work due to the absence of a measurable $^5D_0 \rightarrow {}^7F_6$ transition in the emission spectra. Although this transition is energetically allowed for Eu^{3+} ions, it is typically very weak and located in the near-infrared region (≈750–830 nm), often outside the detection range or below the sensitivity limit of conventional spectroscopic measurements. As a result, emission-based Judd–Ofelt analyses of Eu^{3+} systems commonly rely only on the $^5D_0 \rightarrow {}^7F_2$ and $^5D_0 \rightarrow {}^7F_4$ transitions to determine Ω_2 and Ω_4 parameters, while Ω_6 is generally not reported or is treated as negligible [100,101].

The Ω_2 parameter exhibits a pronounced increase in the Li^+-co-doped sample, confirming a strong enhancement of local asymmetry and Eu–O

Table 9
Radiative (A_{rad}) and non-radiative (A_{nr}) decay rates, radiative and experimental lifetimes, internal quantum efficiency (η), and branching ratios (β_J) of $BaZr(BO_3)_2:Eu^{3+}$ and alkali co-doped samples.

Sample	(A_{rad}) (s^{-1})	(A_{nr}) (s^{-1})	(τ_{rad}) (ms)	(τ_{exp}) (ms)	(η)	(β_2)	(β_4)
$BaZr(BO_3)_2:Eu^{3+}$	180	378.4	5.50	1.785	0.32	0.50	0.06
$+K^+$	200	241.9	5.00	2.263	0.45	0.55	0.06
$+Li^+$	700	−88.4*	1.43	1.637	1.14	0.71	0.07
$+Na^+$	230	286.4	4.30	1.927	0.45	0.52	0.07

covalency. In contrast, the Ω_4 parameter shows only minor variation across all samples, indicating that the long-range structural framework remains largely unchanged. This distinction clearly demonstrates that alkali co-doping primarily modifies the short-range coordination environment around Eu^{3+} ions rather than altering the global crystal structure. These findings are in good agreement with the Rietveld refinement results, which confirm phase purity and structural stability. The total radiative transition rates and lifetimes are presented in Table 9. The branching ratios further support the Judd–Ofelt analysis, with the highest β_2 value observed for the Li^+-co-doped sample, indicating enhanced electric-dipole transition probability and increased local asymmetry around Eu^{3+} ions. In contrast, the K^+-co-doped sample exhibits a comparatively lower β_2 value, consistent with reduced non-radiative losses rather than increased asymmetry being the dominant factor governing its luminescence behavior.

The Li^+-co-doped sample exhibits a significantly higher radiative transition rate, leading to a shorter calculated radiative lifetime. However, this enhancement does not directly translate into the longest experimental lifetime. Instead, the K^+-co-doped sample shows the longest decay time, suggesting that reduced non-radiative losses play a important role in this case. This interpretation is further supported by the calculated non-radiative decay rates. The K^+-co-doped sample exhibits the lowest A_{nr} value (241.9 s^{-1}), which explains its longest experimental lifetime. In comparison, the Na^+-co-doped sample shows a moderately higher A_{nr}, but still lower than that of the Eu^{3+}-only sample, confirming that defect suppression plays a key role in improving luminescence efficiency. It should be noted that the negative A_{nr} value obtained for the Li^+-co-doped sample is not physically meaningful and arises from an overestimation of the radiative transition probability in the emission-based Judd–Ofelt analysis. Consequently, the derived radiative parameters and internal quantum efficiency for this sample should be interpreted qualitatively rather than as absolute values.

The internal quantum efficiency values further support this interpretation. While most samples exhibit physically reasonable values below unity, the Li^+-co-doped sample yields an apparent $\eta > 1$. This unphysical result indicates an overestimation of radiative transition probabilities arising from emission intensity normalization and the inherent limitations of emission-based Judd–Ofelt analysis. In Eu^{3+} systems, emission-derived J–O parameters are known to be sensitive to experimental conditions, limited transition sets, and uncertainties in absolute intensity calibration, which may lead to systematic overestimation of radiative rates [102–104]. Therefore, the calculated η values should be interpreted only in a comparative and qualitative manner rather than as absolute efficiencies. Importantly, the key outcome is the strong enhancement of local asymmetry (high Ω_2) in the Li^+-co-doped sample, while lifetime and thermal analyses reveal the presence of additional non-radiative relaxation pathways that limit the overall luminescence efficiency.

The combined analysis reveals that alkali co-doping plays a dual role in tailoring the photoluminescence properties of $BaZr(BO_3)_2:Eu^{3+}$ phosphors. On one hand, Li^+ co-doping induces a strong distortion of the local coordination environment, significantly enhancing the electric-dipole transition probability and resulting in a substantial increase in the Ω_2 parameter. On the other hand, this strong distortion may simultaneously introduce defect states or local lattice strain that facilitate non-radiative relaxation, thereby limiting the overall luminescence efficiency.

In contrast, K^+ co-doping leads to a more moderate modification of the local symmetry while effectively suppressing non-radiative decay channels, as evidenced by the longer experimental lifetime. This suggests that an optimal balance between symmetry breaking and defect control is required to achieve high luminescence efficiency. The Na^+-co-doped sample exhibits intermediate behavior, indicating a trade-off between these two competing effects.

Therefore, the results demonstrate that maximizing local asymmetry alone is not sufficient for improving luminescence performance. Instead, the interplay between local structural distortion, covalency, and defect chemistry must be carefully controlled. This insight provides a clear strategy for designing high-performance Eu^{3+}-activated borate phosphors through targeted co-doping approaches. The obtained Judd–Ofelt parameters were further compared with previously reported values for $BaZr(BO_3)_2:Eu^{3+}$ phosphors [12]. The Ω_2 and Ω_4 values of the Eu-only, K^+- and Na^+-co-doped samples are in good agreement with literature, confirming the validity of the present emission-based analysis. In particular, the Ω_4 values fall within the typical range reported for borate hosts, indicating that the long-range structural framework remains largely unaffected.

In contrast, the Li^+-co-doped sample exhibits the highest apparent Ω_2 and asymmetry ratio, indicating a strongly distorted and covalent Eu–O environment; however, as discussed above, this value should be interpreted qualitatively. Despite this strong local asymmetry, it is accompanied by a shorter lifetime and moderate thermal stability, suggesting the presence of additional non-radiative channels. In contrast, K^+ co-doping, with moderate Ω_2 and R values, yields the longest lifetime and improved thermal stability, consistent with effective suppression of non-radiative decay pathways. Na^+ co-doping exhibits intermediate Ω_2 values but provides strong emission intensity and the best thermal stability, indicating an optimal balance between symmetry distortion, radiative enhancement, and defect suppression.

These results demonstrate that Ω_2 serves as a useful qualitative indicator of local asymmetry, a higher Ω_2 value does not necessarily correspond to higher luminescence efficiency. Instead, optimal luminescence performance is achieved through a balance between local structural distortion and defect control.

To place the present borate host in context, it is useful to compare its performance with other Eu^{3+}-activated borate matrices. For example, $Sr_2LiScB_4O_{10}:Eu^{3+}$ exhibits intense red emission under 395 nm excitation with suitable CIE coordinates and color purity for WLEDs [52]. $LiBaB_9O_{15}:Eu^{3+}$ shows chromaticity coordinates close to standard red and emission intensities comparable to commercial $Y_2O_3:Eu^{3+}$, depending on the excitation wavelength [105]. Narrow-band $Na_3Y(BO_3)_2:Tb^{3+},Eu^{3+}$ red borates can reach quantum yields up to 83.5% with excellent thermal stability and high color rendering in pc-WLEDs [89]. Compared with these systems, the present Na^+/K^+-compensated borate offers competitive red emission and thermal robustness, while additionally providing a systematic view of alkali-assisted defect control within a single host lattice.

4. Conclusions

This study demonstrates that the $BaZr(BO_3)_2$ host retains its trigonal R3c structure upon Eu^{3+} substitution and alkali co-doping, with only minor local distortions that critically influence the Eu^{3+} emission environment. Concentration-dependent photoluminescence confirms that an optimal Eu^{3+} content of ~3 wt% provides the best balance between emission intensity and concentration quenching, which is governed by long-range dipole–dipole interactions between Eu^{3+} ions. Alkali co-doping effectively compensates the charge imbalance associated with $Eu^{3+} \rightarrow Ba^{2+}$ substitution, suppressing cation vacancies and oxygen-related defects that act as non-radiative recombination centers and thereby enhancing both room-temperature efficiency and thermal robustness. Among the investigated ions, Na^+ delivers the most significant enhancement, yielding approximately twelve-fold higher emission intensity and the strongest retention of luminescence at elevated temperatures, while K^+ provides moderate improvement and Li^+ the weakest effect. Judd–Ofelt analysis and lifetime measurements reveal that optimal luminescence performance is achieved not by maximizing local asymmetry alone, but by establishing an optimal balance between symmetry breaking around Eu^{3+} ions and the suppression of defect-assisted non-radiative processes. Overall, Na^+ and K^+ compensated $BaZr(BO_3)_2:Eu^{3+}$ phosphors are promising red-emitting materials for near-UV/blue-pumped white LEDs. Their luminescence is governed by

the interplay of local structural distortion, charge-compensated defect chemistry, and radiative–nonradiative competition, rather than Ω_2 enhancement alone.

CRediT authorship contribution statement

Can Nurdogan: Writing – review & editing, Writing – original draft, Supervision, Project administration, Methodology, Investigation, Funding acquisition, Conceptualization. **M.B. Coban:** Methodology, Investigation, Formal analysis. **U.H. Kaynar:** Methodology, Investigation, Formal analysis. **B. Tas:** Methodology, Investigation. **H. Aydin:** Software, Methodology, Investigation. **Jabir Hakami:** Software, Methodology, Investigation. **T. Karaman:** Software, Methodology, Investigation. **E.A. Cin:** Software, Methodology, Investigation. **O. Madkhali:** Methodology, Investigation, Conceptualization.

Declaration of Competing Interest

The authors declare that they have no known competing financial interests or personal relationships that could have appeared to influence the work reported in this paper.

Acknowledgements

The authors gratefully acknowledge the funding provided by the Izmir Bakırçay University Scientific Research Projects Coordination Unit under Grant No. TEZ.2025.008.

References

[1] L. Tian, B.-Y. Yu, C.-H. Pyun, H.L. Park, S. Mho, New red phosphors BaZr(BO3)2 and $SrAl_2B_2O_7$ doped with Eu^{3+} for PDP applications, Solid State Commun. 129 (2004) 43–46, https://doi.org/10.1016/j.ssc.2003.09.012.

[2] R. Kiran, V. Shenoy, M.I. Sayyed, A.H. Almuqrin, S.D. Kamath, Judd–Ofelt analysis and the spectroscopic elucidation of β-BaB_2O_4:Eu^{3+} phosphors for optoelectronic applications, RSC Adv. 15 (2025) 43377–43389, https://doi.org/10.1039/D5RA05778G.

[3] I. Ayoub, U. Mushtaq, M.Y.A. Yagoub, S. Som, E. Coetsee, Y.K. Mishra, H. C. Swart, V. Kumar, Structural, optical and photoluminescence properties of $BaLa_2ZnO_5$:Eu^{3+} phosphor: a prospective red-emitting phosphor for LED applications, Opt. Mater. 148 (2024) 114797, https://doi.org/10.1016/j.optmat.2023.114797.

[4] N. Hussain, S. Rubab, V. Kumar, Structure, photoluminescence, Judd-Ofelt analysis, and thermal stability studies of Eu^{3+}-doped $Ba_2Tb_8(SiO_4)_6O_2$ red phosphor with high color purity, Mater. Sci. Eng. B 298 (2023) 116878, https://doi.org/10.1016/j.mseb.2023.116878.

[5] Q. Zhang, X. Wang, X. Ding, Y. Wang, A potential red-emitting phosphor $BaZrGe_3O_9$:Eu^{3+} for WLED and FED applications: synthesis, structure, and luminescence properties, Inorg. Chem. 56 (2017) 6990–6998, https://doi.org/10.1021/acs.inorgchem.7b00591.

[6] I. Charak, M. Manhas, A.K. Bedyal, S. Singh, A. Srivastava, H.C. Swart, V. Kumar, Structural and spectral studies of highly pure red-emitting $Ca_3B_2O_6$:Eu^{3+} phosphors for white light emitting diodes, J. Alloy. Compd. 869 (2021) 159363, https://doi.org/10.1016/j.jallcom.2021.159363.

[7] K. Poria, S. Bhatia, R. Kashyap, V. Kashyap, I. Sihmar, N. Deopa, J.S. Shahi, Structural and luminescence properties of novel Eu^{3+}-doped $Na_3Ba_2LaNb_{10}O_{30}$ phosphors with high quantum efficiency and excellent color purity for w-LED applications, RSC Adv. 14 (2024) 29490–29504, https://doi.org/10.1039/D4RA05026F.

[8] S.K. Gupta, H. Abdou, C.U. Segre, Y. Mao, Excitation-Dependent Photoluminescence of $BaZrO_3$:Eu^{3+} Crystals, Nanomaterials 12 (2022) 3028, https://doi.org/10.3390/nano12173028.

[9] S.C. Lal, A.M. Aiswarya, K.S. Sibi, G. Subodh, Insights into the structure, photoluminescence and Judd-Ofelt analysis of red emitting $SrLaLiTeO_6$:Eu^{3+} phosphors, J. Alloy. Compd. 788 (2019) 1300–1308, https://doi.org/10.1016/j.jallcom.2019.02.260.

[10] P. Kumar, D. Singh, I. Gupta, UV excitable $GdSr_2AlO_5$:Eu^{3+} red emitting nanophosphors: Structure refinement, photoluminescence, Judd-Ofelt analysis and thermal stability for w-LEDs, J. Alloy. Compd. 966 (2023) 171410, https://doi.org/10.1016/j.jallcom.2023.171410.

[11] Z. Liu, Y. Huang, T. Chen, W. Feng, Emission enhancement of Eu^{3+} doped $Ba_2Zn(BO_3)_2$ by adding charge compensators, J. Solid State Chem. 329 (2024) 124431, https://doi.org/10.1016/j.jssc.2023.124431.

[12] Z. Zhang, G. Li, X. Zhang, S. Xu, T. Ji, L. Li, Structural investigation and luminescent properties of $BaZr(BO_3)_2$:Eu^{3+} phosphors containing Si, Chin. Sci. Bull. 55 (2010) 3252–3255, https://doi.org/10.1007/s11434-010-4110-7.

[13] H. Li, J. Zhu, Z. Fang, X. Xiang, J. Jiao, H. Zhang, W. Hu, J. Zhu, Site-selective occupation of Eu^{3+}, high-quenching concentration, and enhanced luminescence via Mg^{2+} co-doping in a borophosphate phosphor, Mater. Today Chem. 30 (2023) 101558, https://doi.org/10.1016/j.mtchem.2023.101558.

[14] B. Li, G. Annadurai, J. Liang, L. Sun, S. Wang, Q. Sun, X. Huang, Lu^{3+} doping induced photoluminescence enhancement in novel high-efficiency $Ba_3Eu(BO_3)_3$ red phosphors for near-UV-excited warm-white LEDs, RSC Adv. 8 (2018) 33710–33716, https://doi.org/10.1039/C8RA07166G.

[15] G. Yuan, R. Cui, J. Zhang, X. Zhang, X. Qi, C. Deng, Photoluminescence evolution and high thermal stability of orange red-emitting $Ba_{3-x}Sr_xZnNb_2O_9$:Eu^{3+} phosphors, J. Solid State Chem. 303 (2021) 122447, https://doi.org/10.1016/j.jssc.2021.122447.

[16] R. Gopal, J. Manam, The photoluminescence and Judd-Ofelt investigations of UV, near-UV and blue excited highly pure red emitting $BaWO_4$:Eu^{3+} phosphor for solid state lighting, Ceram. Int. 49 (2023) 28118–28129, https://doi.org/10.1016/j.ceramint.2023.06.063.

[17] C. Kumari, J. Manam, S. K Sharma, Study of photoluminescence behaviors and Judd-Ofelt analysis of Eu^{3+} doped double perovskite Ba_2GdSbO_6 phosphor for highly pure and strong red-light generation, J. Lumin 263 (2023) 119983, https://doi.org/10.1016/j.jlumin.2023.119983.

[18] Z. Guo, H. Jiang, H. Li, H. Zhang, C. Liu, R. Zhao, Z. Yang, H. Tang, J. Li, J. Zhang, J. Zhu, Manipulating alkali charge compensation to improve red fluorescence and thermostability in $Ba_5P_6O_{20}$:Eu^{3+} phosphor, Appl. Mater. Today 37 (2024) 102095, https://doi.org/10.1016/j.apmt.2024.102095.

[19] H. Tang, M. Chen, X. Zhang, Z. Bai, X. Liu, Q. Liu, Effect of charge compensators (Li^+, Na^+, K^+,Rb^+,Cs^+) on the luminescence properties of $Na_4CaSi_3O_9$:Eu^{3+} red phosphor, Mater. Res. Bull. 184 (2025) 113255, https://doi.org/10.1016/j.materresbull.2024.113255.

[20] Y.-N. Li, D. Zhao, L.-Y. Shi, S.-J. Dai, Y.-P. Fan, B.-Z. Liu, Q.-X. Yao, Enhanced luminescence of a new red phosphor $Na_{13}Sr_2Ta_2(PO_4)_9$:Eu^{3+} by co-doping charge compensators Li^+/Na^+/K^+, J. Lumin 220 (2020) 116976 https://doi.org/10.1016/j.jlumin.2019.116976.

[21] X. Gao, W. Zhang, X. Wang, X. Huang, Z. Zhao, Charge compensation effects of alkali metal ions M^+ (Li^+, Na^+, K^+) on luminescence enhancement in red-emitting $Ca_3Si_2O_7$:Eu^{3+} phosphors, J. Alloy. Compd. 893 (2022) 162265, https://doi.org/10.1016/j.jallcom.2021.162265.

[22] S.K. Gupta, K. Sudarshan, A.K. Yadav, R. Gupta, D. Bhattacharyya, S.N. Jha, R. M. Kadam, Deciphering the Role of Charge Compensator in Optical Properties of $SrWO_4$:Eu^{3+}:A (A = Li^+,Na^+,K^+): spectroscopic insight using photoluminescence, positron annihilation, and X-ray Absorption, Inorg. Chem. 57 (2018) 821–832, https://doi.org/10.1021/acs.inorgchem.7b02780.

[23] Z. Yang, L. Yang, Y. Pu, D. Zhu, The effect and mechanism of different charge compensation on the luminescent properties of Eu-doped $BaSiO_3$ phosphor calcined in air with self-reduction, Opt. Mater. (Amst.). 114 (2021) 110981, https://doi.org/10.1016/j.optmat.2021.110981.

[24] R. Chatterjee, S. Saha, D. Sen, K. Panigrahi, U.K. Ghorai, G.C. Das, K. K. Chattopadhyay, Neutralizing the Charge Imbalance Problem in Eu^{3+}-Activated $BaAl_2O_4$ Nanophosphors: Theoretical Insights and Experimental Validation Considering K^+ Codoping, ACS Omega 3 (2018) 788–800, https://doi.org/10.1021/acsomega.7b01525.

[25] A.S. Altowyan, S.C. Kaynar, H. Aydin, U.H. Kaynar, M.B. Coban, J. Hakami, A. Canimoglu, Y. Ozcan, N. Can, Anomalous $^5D_0 \rightarrow {}^7F_4$ transition induced by alkali ion co-doping in Eu^{3+}-activated $K_7SrY_2(B_5O_{10})_3$ borates: a Judd–Ofelt and photoluminescence analysis for pc-WLEDs, Spectrochim. Acta Part A Mol. Biomol. Spectrosc. 346 (2026) 126870, https://doi.org/10.1016/j.saa.2025.126870.

[26] Q. Li, Y.F. Zhang, Q. Liu, Z.L. Wang, C. Ju, Enhanced red emission of 1D $CaYAl_3O_7$:Eu^{3+} phosphor via co-doping Sm^{3+} or Li^+ /Na^+ /K^+ prepared by electrospinning, Dig. J. Nanomater. Biostruct. 15 (2020) 1153–1164, https://doi.org/10.15251/DJNB.2020.154.1153.

[27] X. Chen, L. Zhao, X. Chang, W. Xiao, Syntheses, crystal structures, vibrational spectra, and luminescent properties of $M_3Eu_2(BO_3)_4$ (M = Ba, Sr), J. Solid State Chem. 283 (2020) 121163, https://doi.org/10.1016/j.jssc.2019.121163.

[28] Y. Deng, Y. Gao, F. Zhu, B. Zhu, L. Huang, J. Qiu, Sol-gel combustion synthesis and near-infrared luminescence of Ni^{2+}-doped $MgAl_2O_4$ spinel phosphor, Ceram. Int. 50 (2024) 12319–12325, https://doi.org/10.1016/j.ceramint.2024.01.136.

[29] L. Junliang, Z. Yanwei, G. Cuijing, Z. Wei, Y. Xiaowei, One-step synthesis of barium hexaferrite nano-powders via microwave-assisted sol–gel auto-combustion, J. Eur. Ceram. Soc. 30 (2010) 993–997, https://doi.org/10.1016/j.jeurceramsoc.2009.10.019.

[30] P. Manju, M.R. Ajith, D. Jaiswal-Nagar, Synthesis and characterization of $BaZrO_3$ nanoparticles by citrate-nitrate sol-gel auto-combustion technique: systematic study for the formation of dense $BaZrO_3$ ceramics, J. Eur. Ceram. Soc. 39 (2019) 3756–3767, https://doi.org/10.1016/j.jeurceramsoc.2019.03.048.

[31] S. Castro, M. Gayoso, J. Rivas, J.M. Greneche, J. Mira, C. Rodríguez, Structural and magnetic properties of barium hexaferrite nanostructured particles prepared by the combustion method, J. Magn. Magn. Mater. 152 (1996) 61–69, https://doi.org/10.1016/0304-8853(95)00450-5.

[32] D.J. Roy, Y.D. Choudhari, K.G. Rewatkar, N.S. Kokode, D.M. Borikar, Investigation of structural and dielectric properties of Co-Zr doped Barium M-type Hexaferrites, J. Phys. Conf. Ser. 1913 (2021) 012056, https://doi.org/10.1088/1742-6596/1913/1/012056.

[33] Z. Ding, X. Huang, W. Liu, I.J. Kim, Y.-H. Han, Preparation of high-temperature active zirconium boride powders via precursor route and microwave sintering, Adv. Appl. Ceram. 120 (2021) 222–226, https://doi.org/10.1080/17436753.2021.1933839.

[34] V. Hornebecq, P. Gravereau, J.P. Chaminade, E. Lebraud, $BaZr(BO_3)_2$: a non-centrosymmetric dolomite-type superstructure, Mater. Res. Bull. 37 (2002) 2165–2178, https://doi.org/10.1016/S0025-5408(02)00899-1.

[35] V.S. Urusov, Cryst. Chem. Energ. Charact. Solid Solut. (1992) 162–193, https://doi.org/10.1007/978-1-4612-2842-4_6.

[36] H. Jiang, A.A. Haider, H. Li, C. Liu, J. Li, H. Zhang, D. Chen, J. Zhu, Substitutional-interstitial synergetic solid solution enables efficient ultra-broadband emission and multicolor luminescence, Laser Photon. Rev. (2026), https://doi.org/10.1002/lpor.202502691.

[37] A. Balhara, S.K. Gupta, G.D. Patra, B. Modak, J. Prakash, K. Sudarshan, M. Mohapatra, Stabilization of Eu^{2+} in $Li_2B_4O_7$ with the BO_3 network through U^{6+} co-doping and defect engineering, Phys. Chem. Chem. Phys. 25 (2023) 1889–1902, https://doi.org/10.1039/D2CP04672E.

[38] A.I. Becerro, M. Allix, M. Laguna, D. González-Mancebo, C. Genevois, A. Caballero, G. Lozano, N.O. Núñez, M. Ocaña, Revealing the substitution mechanism in Eu^{3+}:$CaMoO_4$ and Eu^{3+},Na^{+}:$CaMoO_4$ phosphors, J. Mater. Chem. C. 6 (2018) 12830–12840, https://doi.org/10.1039/C8TC04595J.

[39] A.G. Bispo, D.A. Ceccato, S.A.M. Lima, A.M. Pires, Red phosphor based on Eu^{3+}-isoelectronically doped Ba_2SiO_4 obtained via sol–gel route for solid state lightning, RSC Adv. 7 (2017) 53752–53762, https://doi.org/10.1039/C7RA10494D.

[40] J. Qiao, Z. Xia, Design principles for achieving red emission in Eu^{2+}/Eu^{3+} doped inorganic solids, J. Appl. Phys. 129 (2021), https://doi.org/10.1063/5.0050290.

[41] R.D. Shannon, Revised effective ionic radii and systematic studies of interatomic distances in halides and chalcogenides, Acta Crystallogr. Sect. A 32 (1976) 751–767, https://doi.org/10.1107/S0567739476001551.

[42] X. Yu, Z. Liu, W. Zhang, X. Xu, H. Du, Effect of A^+ (A = Li, Na and K) co-doping on enhancing the luminescence of $Ca_5(PO_4)_2SiO_4$:Eu^{3+} red-emitting phosphors as charge compensator, Ceram. Int. 47 (2021) 3540–3547, https://doi.org/10.1016/j.ceramint.2020.09.198.

[43] N.N. Ahlawat, P. Agamkar, N. Ahlawat, A. Agarwal, Structural Study Of TM Doped Alkali Bismuth Borate Glasses, Adv. Mater. Lett. 4 (2013) 71–73, https://doi.org/10.5185/amlett.2013.icnano.252.

[44] M. Mączka, K. Szymborska-Małek, A. Gągor, A. Majchrowski, Growth and characterization of acentric $BaHf(BO_3)_2$ and $BaZr(BO_3)_2$, J. Solid State Chem. 225 (2015) 330–334, https://doi.org/10.1016/j.jssc.2015.01.008.

[45] K. Marimuthu, S. Surendra Babu, G. Muralidharan, S. Arumugam, C. K. Jayasankar, Structural and optical studies of Eu^{3+} ions in alkali borate glasses, Phys. Status Solidi 206 (2009) 131–139, https://doi.org/10.1002/pssa.200824198.

[46] M.M. El-shabaan, A. Mohamed, M.I. Youssif, N.A. El-Ghamaz, E.M. Ahmed, Comparative study on the influence of rare earth ion doping on the structural and optical properties of simple B_2O_3–Na_2O glasses, Sci. Rep. 15 (2025) 35022, https://doi.org/10.1038/s41598-025-21224-x.

[47] K. Hristova, I.P. Kostova, T.A. Eftimov, G. Patronov, S. Tsoneva, Synthesis and characterization of smartphone-readable luminescent lanthanum borates doped and Co-Doped with Eu and Dy, Photonics 12 (2025) 171, https://doi.org/10.3390/photonics12020171.

[48] R.L. Frost, Raman spectroscopy of selected borate minerals of the pinakiolité group, J. Raman Spectrosc. 42 (2011) 540–543, https://doi.org/10.1002/jrs.2745.

[49] T. Otsuka, R. Oka, M.R. Cicconi, D. de Ligny, T. Hayakawa, Tuning the luminescence color of Eu^{3+}- and alkali-ion-codoped Sr_2CaWO_6 orange-red phosphors: Eu^{3+} site distribution and site-selective photoluminescence studies, APL Mater. 12 (2024), https://doi.org/10.1063/5.0197892.

[50] M. Dimitrievska, T.B. Ivetić, A.P. Litvinchuk, A. Fairbrother, B.B. Miljević, G. R. Štrbac, A. Pérez Rodríguez, S.R. Lukić-Petrović, Eu^{3+}-doped wide band Gap Zn_2SnO_4 semiconductor nanoparticles: structure and luminescence, J. Phys. Chem. C. 120 (2016) 18887–18894, https://doi.org/10.1021/acs.jpcc.6b05335.

[51] M. Beltaif, M. Dammak, M. Megdiche, K. Guidara, Synthesis, optical spectroscopy and Judd–Ofelt analysis of Eu^{3+} doped $Li_2BaP_2O_7$ phosphors, J. Lumin 177 (2016) 373–379, https://doi.org/10.1016/j.jlumin.2016.05.016.

[52] Q. Chen, B. Miao, P.S. Kumar, S. Xu, Enhanced luminescence properties and Judd-Ofelt analysis of novel red emitting $Sr_2LiScB_4O_{10}$:Eu^{3+} phosphors for WLED applications, Opt. Mater. (Amst.). 116 (2021) 111093, https://doi.org/10.1016/j.optmat.2021.111093.

[53] L. Li, W. Chang, W. Chen, Z. Feng, C. Zhao, P. Jiang, Y. Wang, X. Zhou, A. Suchocki, Double perovskite $LiLaMgWO_6$:Eu^{3+} novel red-emitting phosphors for solid sate lighting: Synthesis, structure and photoluminescent properties, Ceram. Int. 43 (2017) 2720–2729, https://doi.org/10.1016/j.ceramint.2016.11.093.

[54] J. Hakami, M.B. Coban, H. Aydin, U.H. Kaynar, M. Sharahili, O. Madkhali, D. Somaily, N. Can, Structural modulation and Judd–Ofelt-guided luminescence enhancement in Eu^{3+}-doped $LiCa_4O(BO_3)_3$ via dual-alkali co-doping, J. Lumin 289 (2026) 121670, https://doi.org/10.1016/j.jlumin.2025.121670.

[55] L. Tian, S.-J. Kim, H.L. Park, S.-I. Mho, Variation of the photoluminescence and vacuum ultraviolet excitation characteristics of $BaZr(BO_3)_2$:Eu^{3+} by the incorporation of Al^{3+}, La^{3+}, or Y^{3+} into the lattice, Mater. Res. Bull. 41 (2006) 29–37, https://doi.org/10.1016/j.materresbull.2005.07.039.

[56] V. Onar, E. Ekdal Karali, A.S. Altowyan, H. Aydin, U.H. Kaynar, C. Gök, M. B. Coban, J. Hakami, Y. Ozcan, A. Canimoglu, N. Can, Luminescence enhancement and thermal stability of alkali co-doped Eu^{3+}:$LaMgB_5O_{10}$ phosphors, Appl. Radiat. Isot. 226 (2025) 112219, https://doi.org/10.1016/j.apradiso.2025.112219.

[57] T. Otsuka, R. Oka, T. Hayakawa, Eu^{3+} Site Distribution and Local Distortion of Photoluminescent Ca_3WO_6:(Eu^{3+},K^{+}) Double Perovskites as High-Color-Purity Red Phosphors, Adv. Sci. 10 (2023), https://doi.org/10.1002/advs.202302559.

[58] S. Jayakiruba, G. Kumar, N. Lakshminarasimhan, Excitation-dependent variation in local symmetry in $Ba_2Mg(BO_3)_2$ evidenced by Eu^{3+} luminescent structural probe, Solid State Sci. 55 (2016) 121–124, https://doi.org/10.1016/j.solidstatesciences.2016.03.001.

[59] G. Rajkumar, V. Ponnusamy, G.V. Kanmani, M.T. Jose, A new perovskite type Ba_2YZrO_6:Eu^{3+} red phosphor with cubical morphology for WLEDs applications, J. Lumin 227 (2020) 117561, https://doi.org/10.1016/j.jlumin.2020.117561.

[60] Y.P. Biryukov, R.S. Bubnova, A.V. Povolotskiy, S.K. Filatov, Synthesis and optical properties of novel red-emitting phosphors $Ba_3Lu_{1-x}Eu_xB_9O_{18}$ (x = 0–0.85), Ceram. Int. 50 (2024) 3491–3496, https://doi.org/10.1016/j.ceramint.2023.11.097.

[61] V.R. Panse, S.P. Hargunani, A. Saregar, S.M. Waghare, A. Hadap, S.V. Dewalkar, Y. Yuberti, Analyzing the photoluminescence and energy transfer in $Sr_3Gd(BO_3)_3$: inorganic borate-based phosphor Eu^{3+}, Tb^{3+} and Ce^{3+}, J. Opt. 55 (2026) 431–440, https://doi.org/10.1007/s12596-024-02077-5.

[62] B. Ribeiro de Mesquita, M.V. dos S. Rezende, M.A. Couto dos Santos, Theoretical and computational investigation of the Eu^{3+} ion local symmetry in fluorides compounds, J. Lumin 238 (2021) 118297, https://doi.org/10.1016/j.jlumin.2021.118297.

[63] L.F. Güleryüz, M. İlhan, Structural, morphological, spectral properties and high quantum efficiency of Eu^{3+}, B^{3+} co-activated double perovskite Ba_2GdMO_6 (M = Nb, Ta) phosphors, Mater. Sci. Eng. B 304 (2024) 117373, https://doi.org/10.1016/j.mseb.2024.117373.

[64] G. Annadurai, B. Devakumar, H. Guo, R. Vijayakumar, B. Li, L. Sun, X. Huang, K. Wang, X.W. Sun, Novel Eu^{3+} -activated $Ba_2Y_5B_5O_{17}$ red-emitting phosphors for white LEDs: high color purity, high quantum efficiency and excellent thermal stability, RSC Adv. 8 (2018) 23323–23331, https://doi.org/10.1039/C8RA03059F.

[65] G. Blasse, Energy transfer in oxidic phosphors, Phys. Lett. A 28 (1968) 444–445, https://doi.org/10.1016/0375-9601(68)90486-6.

[66] A.S. Khobragade, D.H. Gahane, R.T. Maske, B.V. Tupate, A.N. Yerpude, Photoluminescence properties and concentration quenching mechanism of Eu^{3+}-doped $CaLa_2Mo_4O_{16}$ phosphor for red-emitting LED, Luminescence 40 (2025), https://doi.org/10.1002/bio.70157.

[67] U.H. Kaynar, M.B. Coban, J. Hakami, A.S. Altowyan, H. Aydin, M. Ayvacikli, N. Can, Enhanced luminescence of Eu^{3+} in $LaAl_2B_4O_{10}$ via energy transfer from Dy^{3+} doping, Spectrochim. Acta Part A Mol. Biomol. Spectrosc. 321 (2024) 124711, https://doi.org/10.1016/j.saa.2024.124711.

[68] T. Sakthivel, G. Annadurai, R. Vijayakumar, X. Huang, Synthesis, luminescence properties and thermal stability of Eu^{3+}-activated $Na_2Y_2B_2O_7$ red phosphors excited by near-UV light for pc-WLEDs, J. Lumin 205 (2019) 129–135, https://doi.org/10.1016/j.jlumin.2018.09.008.

[69] J. Hong, Y. Liu, Y. Xu, X. Meng, H. Fan, J. Li, Z. Lin, Luminescence properties and energy transfer study of color temperature tunable $CaSrSiO_4$:Dy^{3+},Eu^{3+} white phosphors, Opt. Mater. 149 (2024) 115033, https://doi.org/10.1016/j.optmat.2024.115033.

[70] U.H. Kaynar, H. Aydin, A.S. Altowyan, J. Hakami, M.B. Coban, M. Ayvacikli, E. Ekdal Karali, A. Canimoglu, N. Can, Enhancement of luminescence and thermal stability in Eu^{3+}-doped $K_3Y(BO_2)_6$ with Li^{+} and Na^{+} co-doping, Adv. Powder Technol. 35 (2024) 104695, https://doi.org/10.1016/j.apt.2024.104695.

[71] P.N. Parale, A.R. Kadam, S.J. Dhoble, K.V. Dabre, Tailored efficient energy transfer Tb^{3+}, Eu^{3+} activated/co-activated $LiAl(PO_3)_4$ phosphor by substitution of alkali metals: the effect of charge compensation, RSC Adv. 13 (2023) 26179–26188, https://doi.org/10.1039/D3RA03115B.

[72] F. Ruan, G. Fan, N. Li, J. Zhou, Y. Li, D. Fan, Q. Chen, Z. Lin, Charge compensation effect of alkali metal ions on luminescence enhancement and negative thermal quenching of $Sr_{1-x}LaNaTeO_6$:xEu^{3+} red phosphors, Ceram. Int. 50 (2024) 12866–12876, https://doi.org/10.1016/j.ceramint.2024.01.194.

[73] P. Halappa, A. Mathur, M.-H. Delville, C. Shivakumara, Alkali metal ion co-doped Eu^{3+} activated $GdPO_4$ phosphors: Structure and photoluminescence properties, J. Alloy. Compd. 740 (2018) 1086–1098, https://doi.org/10.1016/j.jallcom.2018.01.087.

[74] Y. Ma, S. Chen, J. Che, J. Wang, R. Kang, J. Zhao, B. Deng, R. Yu, H. Geng, Effect of charge compensators (Li^{+}, Na^{+}, K^{+}) on the luminescence properties of Sr_3TeO_6:Eu^{3+} red phosphor, Ceram. Int. 47 (2021) 8518–8527, https://doi.org/10.1016/j.ceramint.2020.11.219.

[75] D. Liu, Y. Liu, Y. Zhu, S. Ye, Shaojie Bai, Enhancement of luminescence properties of Zn(W–Mo)O_4:Eu^{3+} red phosphors by co-doped charge compensators A^{+}(Li^{+}, Na^{+}, K^{+}), Ceram. Int. 47 (2021) 28021–28031, https://doi.org/10.1016/j.ceramint.2021.06.134.

[76] A.S. Altowyan, U.H. Kaynar, J. Hakami, M.B. Coban, M. Ayvacikli, H. Aydin, A. Canimoglu, N. Can, Integrating K^{+} into Eu and Tb doped $GdCa_4O(BO_3)_3$: a dual study on photoluminescence and structure, Sens. Actuators A Phys. 373 (2024) 115453, https://doi.org/10.1016/j.sna.2024.115453.

[77] H. Li, Y. Niu, C. Liu, H. Jiang, J. Li, J. Wu, S. Huang, H. Zhang, J. Zhu, Unraveling the remarkable influence of square antiprism geometry on highly efficient far-red emission of Eu^{3+} in borotellurate phosphors for versatile utilizations, Laser Photon. Rev. 18 (2024), https://doi.org/10.1002/lpor.202400843.

[78] H. Li, A.A. Haider, Z. Xie, C. Liu, H. Zhang, H. Jiang, J. Li, J. Zhu, Synergetic contributions of high quenching concentration and tuned square antiprism geometry boosting far-red emission of Eu^{3+} with near-unit efficiency, Adv. Sci. 12 (2025), https://doi.org/10.1002/advs.202415989.

[79] S. Liu, Y. Liang, Y. Zhu, H. Li, J. Chen, M. Wang, W. Li, Enhancing emission intensity and thermal stability by charge compensation in $Sr_2Mg_3P_4O_{15}$:Eu^{3+}, J. Am. Ceram. Soc. 101 (2018) 1655–1664, https://doi.org/10.1111/jace.15334.
[80] L. Wu, S. Sun, Y. Bai, Z. Xia, L. Wu, H. Chen, L. Zheng, H. Yi, T. Sun, Y. Kong, Y. Zhang, J. Xu, Defect-induced self-reduction and anti-thermal quenching in $NaZn(PO_3)_3$:Mn^{2+} red phosphor, Adv. Opt. Mater. 9 (2021), https://doi.org/10.1002/adom.202100870.
[81] C. Wang, Y. Cai, H. Zhang, Z. Liu, H. Lv, X. Zhu, Y. Liu, C. Wang, J. Qiu, X. Yu, X. Xu, Variation from zero to negative thermal quenching of phosphor with assistance of defect states, Inorg. Chem. 60 (2021) 19365–19372, https://doi.org/10.1021/acs.inorgchem.1c03188.
[82] H. Su, X. Li, D. Li, D. Gao, M. Zhang, Y. Shang, Y. Liu, H. Geng, X. Liu, R. Yu, Strategic point defect engineering toward abnormal thermal quenching in Sm^{3+}-doped Na-rich $Na_{1.5}La_{1.5}TeO_6$ phosphors for LEDs applications, Ceram. Int. 50 (2024) 34111–34122, https://doi.org/10.1016/j.ceramint.2024.06.230.
[83] Y. Gao, X. Zhu, H. Shi, P. Jiang, R. Cong, T. Yang, Eu^{3+} and Tb^{3+} doped $LiCaY_5(BO_3)_6$: efficient red and green phosphors under UV or NUV excitations, J. Lumin 242 (2022) 118598, https://doi.org/10.1016/j.jlumin.2021.118598.
[84] H. Guo, L. Sun, J. Liang, B. Li, X. Huang, High-efficiency and thermal-stable Eu^{3+}-activated $Ca_3Y(AlO)_3(BO_3)_4$ red-emitting phosphors for near-UV-excited white LEDs, J. Lumin 205 (2019) 115–121, https://doi.org/10.1016/j.jlumin.2018.09.010.
[85] O. Madkhali, Ü.H. Kaynar, S. Cam Kaynar, M. Ayvacikli, N. Can, Dy^{3+} and Eu^{3+} co-activated gadolinium aluminate borate phosphor: synthesis, enhanced luminescence, energy transfer and tunable color, Mater. Res. Bull. 164 (2023) 112282, https://doi.org/10.1016/j.materresbull.2023.112282.
[86] S. Ren, X. Kong, M. Wei, Z. Wang, Y. Liu, B. Dierre, R. Abellon, H.T. Hintzen, Concentration-Quenching-Suppressed Eu^{3+}-Activated $Ba_3Lu_2B_6O_{15}$ orange-red-emitting phosphors via one-dimensional structural confinement for thermally stable white LEDs, Inorg. Chem. 64 (2025) 18588–18598, https://doi.org/10.1021/acs.inorgchem.5c03366.
[87] K. Singh, M. Rajendran, R. Devi, S. Vaidyanathan, Narrow-band red-emitting phosphors with high color purity, trifling thermal and concentration quenching for hybrid white LEDs and $Li_3Y_3BaSr(MoO_4)_8$:Sm^{3+},Eu^{3+}-based deep-red LEDs for plant growth applications, Inorg. Chem. 61 (2022) 2768–2782, https://doi.org/10.1021/acs.inorgchem.1c02836.
[88] M.T. Tran, N. Van Quang, N.T. Huyen, N. Tu, N. Van Du, D.Q. Trung, N.T. Tuan, N.D. Hung, D.X. Viet, D.T. Tung, N.D. Trung Kien, T.T. Hao Tam, P.T. Huy, High quantum efficiency and excellent color purity of red-emitting Eu^{3+} -heavily doped $Gd(BO_2)_3$-Y_3BO_6-$GdBO_3$ phosphors for NUV-pumped WLED applications, RSC Adv. 13 (2023) 25069–25080, https://doi.org/10.1039/D3RA03955B.
[89] T. Wang, Q. Shi, K.V. Ivanovskikh, L. Wang, H. Guo, P. Huang, C. Cui, A potential high color purity and thermally stable red-emitting phosphor based on Tb^{3+} and Eu^{3+} co-doped sodium yttrium borate: synthesis and luminescence spectroscopic characterization, J. Lumin 236 (2021) 118138, https://doi.org/10.1016/j.jlumin.2021.118138.
[90] S. Wang, Q. Sun, B. Devakumar, J. Liang, L. Sun, X. Huang, Novel high color-purity Eu^{3+}-activated $Ba_3Lu_4O_9$ red-emitting phosphors with high quantum efficiency and good thermal stability for warm white LEDs, J. Lumin 209 (2019) 156–162, https://doi.org/10.1016/j.jlumin.2019.01.050.
[91] X. Wu, X. Zhao, Q. Ren, L. Du, M. Pei, O. Hai, Tuning of emission by effect of local symmetry in $BaLaLiWO_6$:Dy^{3+}/Eu^{3+} for WLEDs, Ceram. Int. 48 (2022) 18793–18802, https://doi.org/10.1016/j.ceramint.2022.03.155.
[92] P. Dai, X. Zhang, L. Bian, S. Lu, Y. Liu, X. Wang, Color tuning of $(K_{1-x},Na_x)SrPO_4$: $0.005Eu^{2+}$, yTb^{3+} blue-emitting phosphors via crystal field modulation and energy transfer, J. Mater. Chem. C. 1 (2013) 4570, https://doi.org/10.1039/c3tc30128a.
[93] Y.-H. Wang, Y.-J. Chen, X.-J. Geng, Y. Yang, Z.-Q. Li, X.-Y. Zuo, Effect of heavy-doping Eu^{3+} and charge compensation on crystalline phase and luminescence properties of $K_2CaP_2O_7$ phosphors emitting orange-red light, J. Chem. Sci. 136 (2024) 16, https://doi.org/10.1007/s12039-024-02251-z.
[94] B.R. Judd, Optical absorption intensities of rare-earth ions, Phys. Rev. 127 (1962) 750–761, https://doi.org/10.1103/PhysRev.127.750.
[95] G.S. Ofelt, Intensities of crystal spectra of rare-earth ions, J. Chem. Phys. 37 (1962) 511–520, https://doi.org/10.1063/1.1701366.
[96] P. Van Do, V.P. Tuyen, V.X. Quang, N.T. Thanh, V.T.T. Ha, H. Van Tuyen, N. M. Khaidukov, J. Marcazzó, Y.-I. Lee, B.T. Huy, Optical properties and Judd–Ofelt parameters of Dy^{3+} doped K_2GdF_5 single crystal, Opt. Mater. 35 (2013) 1636–1641, https://doi.org/10.1016/j.optmat.2013.04.014.
[97] J.D.L. Dutra, N.B.D. Lima, R.O. Freire, A.M. Simas, Europium luminescence: electronic densities and superdelocalizabilities for a unique adjustment of theoretical intensity parameters, Sci. Rep. 5 (2015) 13695, https://doi.org/10.1038/srep13695.
[98] A. Ćirić, Ł. Marciniak, M.D. Dramićanin, Self-referenced method for the Judd–Ofelt parametrisation of the Eu^{3+} excitation spectrum, Sci. Rep. 12 (2022) 563, https://doi.org/10.1038/s41598-021-04651-4.
[99] A.A. El-Maaref, K.S. Shaaban, E.A. Abdel Wahab, Structural, physical, and Judd-Ofelt analysis of germanium magnesium-telluroborate glass containing different amounts of Tm_2O_3, Ceram. Int. (2024), https://doi.org/10.1016/j.ceramint.2024.11.487.
[100] M. De, S. Jana, S. Mitra, Structural and spectroscopic characteristics of Eu^{3+} embedded titanium lead phosphate glasses for red luminescence, Solid State Sci. 114 (2021) 106560, https://doi.org/10.1016/j.solidstatesciences.2021.106560.
[101] M. Sahu, R.K. Verma, Luminescence of Eu^{3+}/Eu^{2+} In PVA film: transitions from the 5D0 level and its lifetime measurement, Prabha Mater. Sci. Lett. 4 (2025) 170–178, https://doi.org/10.33889/PMSL.2025.4.2.016.
[102] C. Yu, X. Zhang, X. Li, J. Zhang, S. Xu, X. Zhang, Y. Zhang, X. Wang, L. Wang, G. Sui, B. Chen, Determination of Judd-Ofelt parameters for Eu^{3+}-doped alkali borate glasses, Mater. Res. Bull. 120 (2019) 110590, https://doi.org/10.1016/j.materresbull.2019.110590.
[103] M. Gopinath, R. J, S. Gopi, S.M. Simon, A.C. Saritha, P.R. Biju, C. Joseph, N. V. Unnikrishnan, Spectroscopic analysis of Eu $^{3+}$ doped silica–titania–polydimethylsiloxane hybrid ORMOSILs, RSC Adv. 10 (2020) 20057–20066, https://doi.org/10.1039/D0RA03073B.
[104] E. Cantelar, J.A. Sanz-García, A. Sanz-Martín, J.E. Muñoz Santiuste, F. Cussó, Structural, photoluminescent properties and Judd-Ofelt analysis of Eu^{3+}-activated CaF_2 nanocubes, J. Alloy. Compd. 813 (2020) 152194, https://doi.org/10.1016/j.jallcom.2019.152194.
[105] W. Zhang, Y. Chen, X. Geng, Y. Yang, L. Xiao, Synthesis and luminescence properties of $LiBaB_9O_{15}$:Eu^{3+} single-component red-light emitting phosphors, J. Lumin 224 (2020) 117324, https://doi.org/10.1016/j.jlumin.2020.117324.